



**Michigan
Technological
University**

Michigan Technological University
Digital Commons @ Michigan Tech

Dissertations, Master's Theses and Master's Reports

2016

Nd₂Fe₁₄B: (Nd_{1-x} Dy_x)₂ Fe₁₄B CORE-SHELL STRUCTURE FORMATION BY HOT PRESS LIQUID PHASE SINTERING

Li Chen

Michigan Technological University, lchen2@mtu.edu

Copyright 2016 Li Chen

Recommended Citation

Chen, Li, "Nd₂Fe₁₄B: (Nd_{1-x} Dy_x)₂ Fe₁₄B CORE-SHELL STRUCTURE FORMATION BY HOT PRESS LIQUID PHASE SINTERING", Open Access Master's Thesis, Michigan Technological University, 2016.
<https://doi.org/10.37099/mtu.dc.etdr/76>

Follow this and additional works at: <https://digitalcommons.mtu.edu/etdr>



Part of the [Metallurgy Commons](#)

Nd₂Fe₁₄B: (Nd_{1-x} Dy_x)₂ Fe₁₄B CORE-SHELL STRUCTURE FORMATION BY HOT
PRESS LIQUID PHASE SINTERING

By

Li Chen

A THESIS

Submitted in partial fulfillment of the requirements for the degree of

MASTER OF SCIENCE

In Materials Science and Engineering

MICHIGAN TECHNOLOGICAL UNIVERSITY

2016

©2016 Li Chen

This thesis has been approved in partial fulfillment of the requirements for the Degree of
MASTER OF SCIENCE in Materials Science and Engineering.

Department of Materials Science and Engineering

Thesis Advisor: *Stephen A. Hackney*

Committee Member: *Stephen L. Kampe*

Committee Member: *Peter D. Moran*

Committee Member: *Ravindra Pandey*

Table of Contents

Abstract.....	iv
Chapter 1 Introduction	1
2.1 Background.....	3
2.2 Statement of Objective and Hypothesis.....	7
Chapter 3 Experimental Methods	9
3.1 Powder Preparation and Handling	9
3.2 Hot Press Process.....	13
3.3 Microstructure Analysis.....	16
3.4 Coefficient of variance *.....	18
3.5 Error Analysis	20
Chapter 4 Experiment Results Analysis and Discussion	24
4.1 Microstructure and Chemistry of Two Alloy Sintered Materials.....	24
4.2 Sintering and Hot Pressing Experiment Matrix.....	29
4.3 Microstructural Evidence of Dy Composition Core Shell Structure	32
4.4 Analysis and Discussion of Results.	43
4.5 Determination of Mechanism Activation Energies.....	46
4.6 Analysis of Hypothesis	49
Chapter 5 Conclusion.....	53
References.....	55
Appendix A Time, temperature and process comparison of experiment matrix.....	59
Appendix B The analysis of Ψ in equation 4.8(a)	61
Appendix C Copyright permission for Figure 2.1	64

Abstract

The purpose of this project is to produce Nd rich core-Dy rich shell grain structure in liquid phase sintered alloys by consolidating Dy rich powder mixed with $\text{Nd}_2\text{Fe}_{14}\text{B}$ powder. The technical barrier to producing the core-shell microstructure is that the Dy composition variations will homogenize during the consolidation process. This dissertation is based on the hypothesis that compositional homogenization of the core-shell structure can be minimized if consolidation occurs under applied pressure (hot press liquid phase sintering). The hypothesis is tested by comparing the homogenization of the Dy composition to the degree of consolidation with and without applied pressure. It is demonstrated that Nd rich core-Dy rich shell grain structure can be produced using the hot press approach. A simple linear model is used to identify the critical processing parameters involved in the successful development of the requisite core-shell structure.

Chapter 1 Introduction

Rare earth magnets based on the stoichiometry $(\text{Nd})_2\text{Fe}_{14}\text{B}$ have large coercivity and a large BH product and are thus attractive for utilization in electric vehicle motors [1]. The elevated temperature environment of an electric vehicle drive train requires the use of heavy rare earth elements to raise the Curie temperature and stabilize the coercivity [2]. A typical rare earth (RE) magnet chemistry capable of operating in an electric motor at the required $\sim 160^\circ\text{C}$ is $\text{Nd}_2\text{Fe}_{14}\text{B}$ [3]. The recent dramatic but temporary increase in heavy rare earth prices due to export controls introduced in China [4] has led to efforts to minimize the impact of future political or economic disruptions in heavy rare earth supply. For high temperature magnet manufacturers and end users, this has translated into efforts in materials design/processing to reduce the amount of Dy used for high temperature magnets without sacrificing magnetic properties. A recent successful approach has been to produce polycrystalline alloys that have grain boundaries enriched in Dy while the grain core has much less Dy. The resulting Nd rich grain core-Dy rich boundary shell appears to create an acceptable BH product at 160°C while using significantly less Dy than required when the alloy is homogeneous in Dy [2]. The operating mechanism for the improved performance of the core-shell structure has been proposed as the inhibition of magnetic domain reversal initiated at the grain

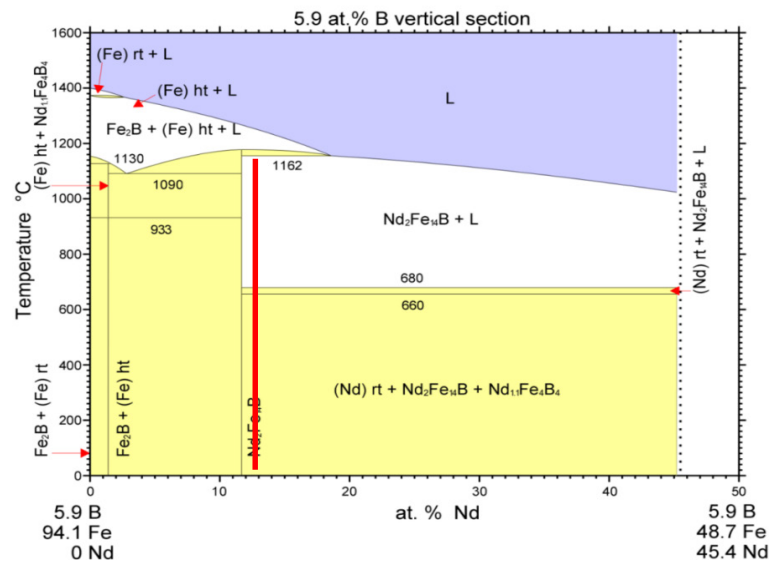
boundaries [5]. That is, the area of the sample that has the lowest barrier for nucleation of domains that can reverse the direction of magnetization has been enriched with an element that tends to prevent the initiation of domain reversal.

The materials processing route currently being used to produce the proposed $\text{Nd}_2\text{Fe}_{14}\text{B}:(\text{Nd}_{1-x}\text{Dy}_x)_2\text{Fe}_{14}\text{B}$ compositional core shell grain microstructure is grain boundary diffusion into the bulk of the magnet during vapor deposition of Dy on the surface [2]. The purpose of the investigation presented here is to test the hypothesis that compositional core-shell $\text{Nd}_2\text{Fe}_{14}\text{B}:(\text{Nd}_{1-x}\text{Dy}_x)_2\text{Fe}_{14}\text{B}$ grain structures could be produced during powder processing/consolidation of a mixture of Dy rich powder and Nd rich powder by optimizing the processing conditions. Specifically, if the alloy homogenization rate could be reduced relative to the powder consolidation rate, then a core shell structure will be developed because fast grain boundary diffusion during consolidation will disperse Dy on the grain boundaries but consolidation will be complete before the slow volume diffusion will allow homogenization.

Chapter 2 Background, Objective and Hypothesis

2.1 Background

The current process used to make bulk $(RE)_2Fe_{14}B$ based magnets uses liquid phase sintering of alloy powder with composition just off the 2:14:1 stoichiometry. A slight excess in RE content produces liquid: solid mixture above 660 °C in NdFeB alloys. Although the quaternary Dy:Nd:Fe:B phase diagrams are not published, a similar two phase liquid: solid mixtures are also found at moderate temperatures in the 4 component alloy [6].



© ASM International 2006. Diagram No. 978568

Figure 2.1 Nd-Fe-B Phase diagram with red line and red arrow showing the composition and the temperature used in liquid sintering [7].

Rare earth elements are extremely sensitive to oxidation processes and all powder preparation processes and heat treatments must be carried out in reducing atmospheres or under vacuum [8].

The heavy rare earth Dy substitutes for Nd in the single phase $(\text{RE})_2\text{Fe}_{14}\text{B}$ crystal structure to give $(\text{Dy}_x\text{Nd}_{1-x})_2\text{Fe}_{14}\text{B}$ [9] which is analogous to quasi-binary solid solution behavior (Cu-Ni).

The addition of Dy increases the room temperature and elevated value of the coercivity H_{ci} , and energy product, BH [1, 2]. A theory has been proposed that similar advantages in Dy containing $(\text{RE})_2\text{Fe}_{14}\text{B}$ magnets can be obtained if the Dy is added only at the grain boundaries in $(\text{Dy}_x\text{Nd}_{1-x})_2\text{Fe}_{14}\text{B}$ [1, 2]. Hitachi has developed a process for Dy addition primarily on the grain boundaries of the in Nd-Fe-B based sintered magnet using Dy diffusion from the surface of the magnet at a temperature where grain boundary diffusion is much faster than volume diffusion [1, 2].

Cross-sectional view schematically illustrating the configuration of the patented process vessel that is used by Hitachi for producing an RE-Fe-B based rare earth sintered magnet with heavy RE enriched grain boundaries [2].

The diffusion of Dy into the bulk magnet, primarily along the grain boundaries, occurs as Dy is being deposited from the vapor phase onto the surface. The process is

proposed to develop a structure for the case where the diffusion length along the boundary is much greater than the diffusion length through the grain $\sqrt{D_B t} \gg \sqrt{D t}$ [2].

Post process analysis by Hitachi does indeed suggest that the proposed grain boundary enrichment in Dy has occurred, with energy dispersive spectroscopy (EDS) analysis of magnet cross sections at the grain boundary triple junctions [2] showing the Dy concentration in the grain center is lower than in the grain boundary triple junction at 50 μm and 500 μm depth from sample surface.

The research partners at GM for this project have carried out Dy element mapping on cross sections of Hitachi processed magnets pulled from a Toyota Prius electric motor (figure 2.2). These element mapping studies confirm the structure suggested by the local EDS results of Hitachi [2].

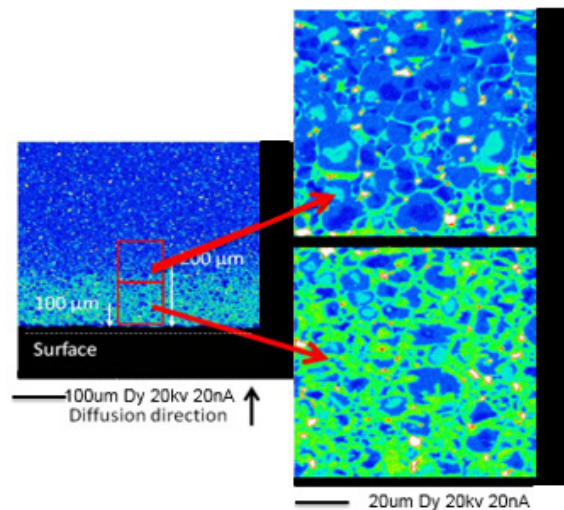


Figure 2.2 Electron Microprobe EDS Dy distribution map for Toyota Prius C magnet

showing Dy localization on the grain boundaries (green) while relatively low Dy concentration exists within the grain center (blue) (obtained by Wakade and Waldo, GM)

In Figure 2.3, coercivity data from magnets produced by the grain boundary diffusion/enrichment process (material and data provided by GM) is examined. The ICP data for the composition of the bulk magnets before and after the grain boundary diffusion/enrichment process and the change of magnetic properties were provided to GM by the manufacturer. The results are shown in Figure 2.3. The blue arrows are indicative of the derivative $\frac{d(H_{cj})}{d(Dy \text{ wt}\%)}$ magnitude change due to the grain boundary diffusion/enrichment process for each lot.

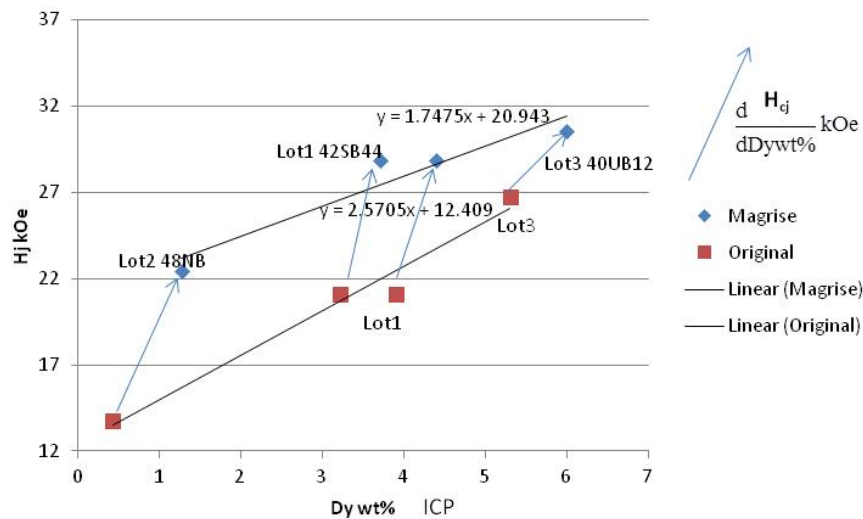


Figure 2.3 Magnet properties change with Dy wt% and grain boundary diffusion/enrichment process

The Hitachi method requires a significant investment in vacuum processing equipment of \$4 million [10] and also adds additional processing steps after the consolidation process. The approach to be pursued in the present investigation is the use of blended powders (or pieces) of Dy rich alloy and powders of Nd rich alloy, known as the "two alloy method"[5] and has proved problematic in the past because of Dy homogenization during consolidation.

This is summarized by Shin-Etsu as "*With the conventional Two Alloy Method, since the dysprosium is diffused during sintering at high temperatures, the dysprosium is distributed widely in the interior of grains, and so an excess of dysprosium is necessary*"[5]. Published evidence of almost complete Dy homogenization within the $(RE)_2Fe_{14}B$ grain during liquid phase sintering of mixed composition powders to full density is also demonstrated by Li et al [9].

2.2 Statement of Objective and Hypothesis.

The problem of homogenization of Dy during consolidation of mixed powders is illustrated in Figure 2.4 together with the objective of this work, which is to achieve Nd rich core-Dy rich shell grain structure during consolidation (left hand branch of figure 2.4). It is apparent that the traditional liquid phase sintering consolidation approach occurs together with compositional homogenization in mixed Dy rich-Nd rich powders.

That is the right hand branch is favored. The hypothesis examined in this thesis is that if the consolidation of can be carried out under applied pressure (hot pressing) then the two alloy method can be used to produce a compositional core shell structure because the consolidation rate is accelerated under applied pressure relative to the homogenization rate.

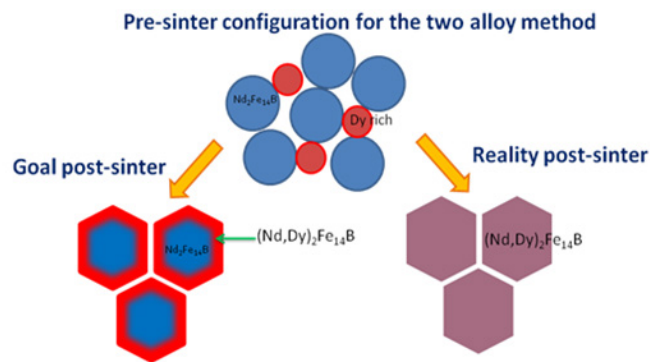


Figure 2.4 Two alloy process compare with Hitachi process

Chapter 3 Experimental Methods

3.1 Powder Preparation and Handling

The preparation of the Nd rich powder follows processes described in detail in the literature. The Nd rich powder is formed by melting together stock materials having compositions 71.18 wt% $\text{Nd}_2\text{Fe}_{14}\text{B}$, 8.805 wt% Nd, 17.917 wt% Fe, 1.417 wt% Co, 0.628 wt% Ga to produce a stoichiometry of $\text{Nd}_{2.6}(\text{FeCo})_{14}\text{BGa}_{0.1}$. The stock materials are melted together in quartz crucible in an induction heating furnace. The resulting alloy ingot is then melt spun (>1600 K, tested by infrared thermometer) into ribbons with the drum velocity set at 2.5m/s. The ribbons are embrittled and transformed into a powder in H_2 atmosphere using the standard hydrogenation, disproportionation, desorption, and recombination (HDDR) process [References] at a temperature of 200°C . Ribbons break up into flakes after the HDDR. After degassing, the HDDR processed material is spec milled at low energy [References]. The effect of HDDR on the powder structure is shown in figure 3.1, where it is demonstrated that the HDDR process allows for a finer particle size after low energy milling than low energy milling without HDDR processing. This indicates the HDDR process allows for fine powder development without overt loss of crystallinity that would result from high energy milling.

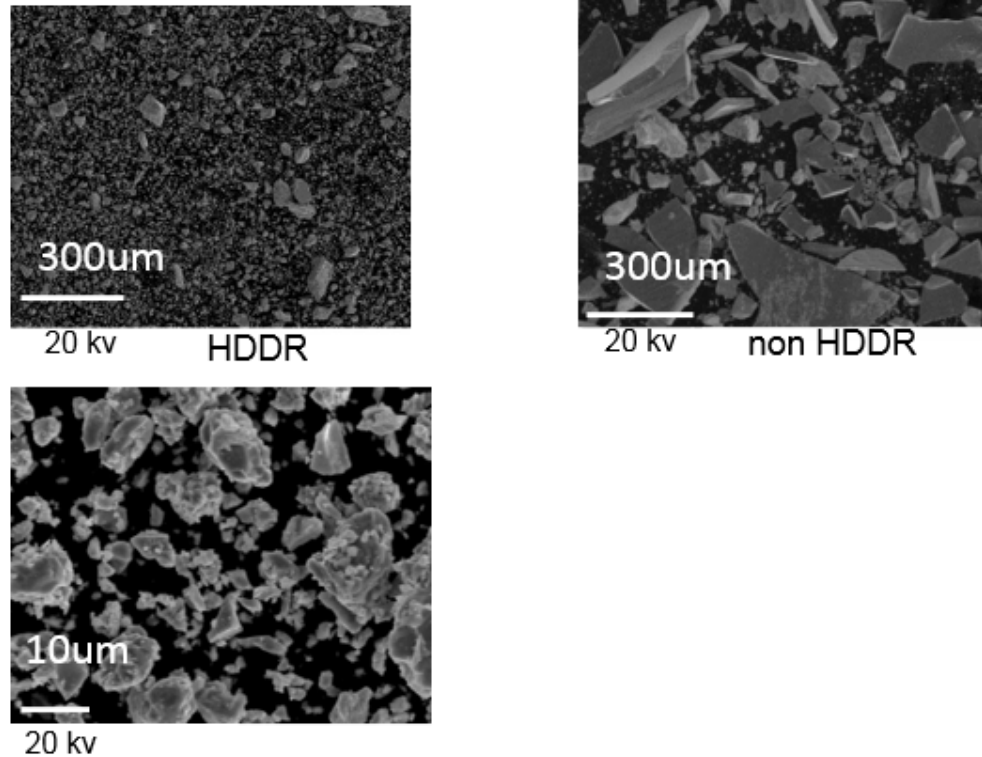


Figure. 3.1 Spex mill Nd₂Fe₁₄B ribbon for 15 minutes with 1 1/4 inch steel ball.

Compare Nd₂Fe₁₄B powder with HDDR process and Nd₂Fe₁₄B powder without HDDR process.

All powder handling, including milling and cold compaction, were carried out in an inert atmosphere glove box. Attempts to process rare earth materials in are result in heavy oxidation of the rare earth elements, with the possibility of extreme thermal events.

The ribbons were spex milled for 50 minutes to fine powder using 0.25 inch steel balls with a media to mill ratio of 1/17. The Dy rich powder was prepared from in a

similar manner from spex milling of melt spun (50 m/s) $\text{Dy}_{2.34}\text{Fe}$ ingot or from $\text{Dy}_{2.34}\text{Fe}$ ingot alloyed to produce $\text{Dy}_2\text{Fe}_{14}\text{B}$. The $\text{Dy}_{25}\text{Fe}_{14}\text{B}$ source material is made by high energy milling of $\text{Dy}_{2.34}\text{Fe}$ commercial ingots, Fe powder and B powder in a spex mill with 2 ½ inch diameter steel balls for 45 minutes to find powder. Mill media/material ratio of 1/1.1.

Table 3.1 Dy source preparation

	Dy source milling process			
Hot pressed sample	mill with 1 1/4 in ball	mill time(mins)	mill with 2 1/2 in ball	mill time(mins)
	Media/Material		Media/Material	
95% as pressed	1/17	50	1/1.1	15
99% as pressed	-----	-----	1/1.1	45
97% as pressed	1/17	50	1/1.1	60
sintered sample	mill with 1 1/4 in ball	mill time(mins)	mill with 2 1/2 in ball	mill time(mins)
	Media/Material		Media/Material	
875 5h	1/17	50	-----	-----
900 5h	1/17	50	-----	-----
925 5h	1/17	50	-----	-----
1050 30m	-----	-----	1/1.1	30
1050 5h FP	-----	-----	1/1.1	30
1050 5h PP	1/17	50	-----	-----
675	1/17	50	-----	-----

There are two milling processes in powder preparation, high energy milling and low energy. High energy milling uses two 1/2 inch steel balls. Mill media for high energy milling is 1/1.1 (Media/Material). Low energy milling uses one 1/4 inch steel ball. Mill media for low energy milling is 1/17 (Media/Material). The differences for these two milling process are shown in figure 3.1 and figure 3.2.

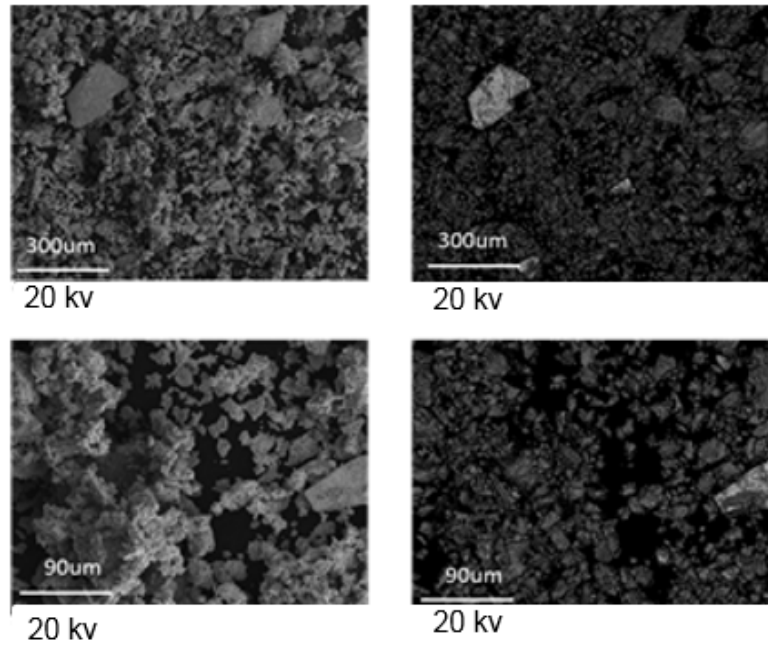


Figure. 3.2 $\text{Nd}_2\text{Fe}_{14}\text{B}$ ribbon and $\text{Dy}_{2.34}\text{Fe}$ ribbon mill with 1 ¼ ball 50mins.

1/17 (Media/Material)

Figure 3.2 shows with low energy mill through whole milling process, milling is not sufficient. $\text{Dy}_{2.34}\text{Fe}$ powder size is too large and Dy source didn't distribute homogeneous.

Powder size shows in figure 3.3 indicates the mixed milling process (high energy and low energy) is efficient compare single milling process.

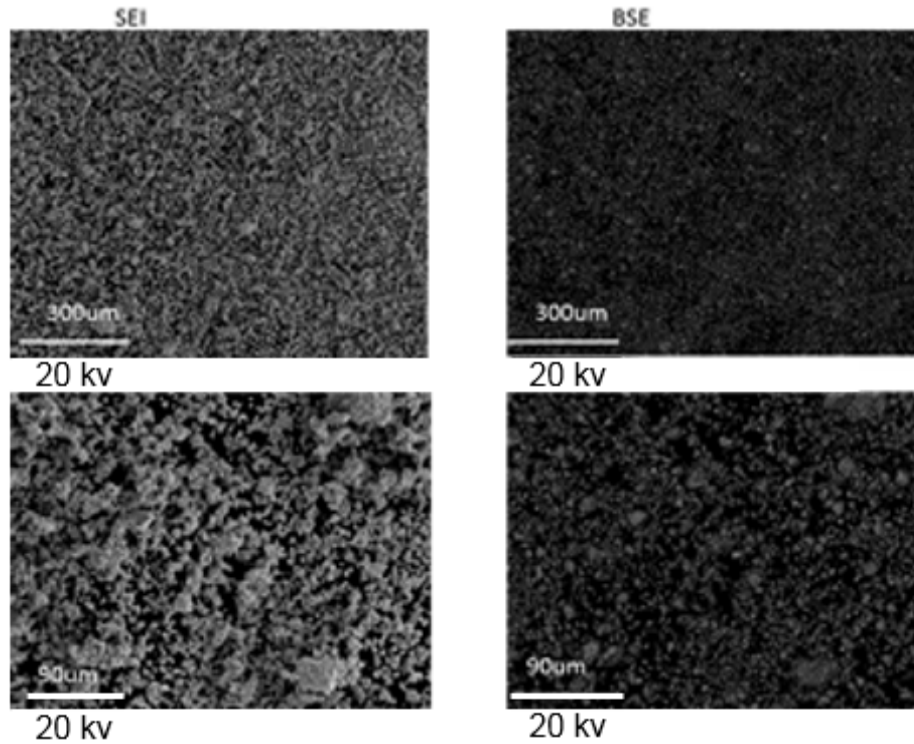


Figure. 3.3 $\text{Nd}_2\text{Fe}_{14}\text{B}$ ribbon and $\text{Dy}_{2.34}\text{Fe}$ ribbon mill with 1 $\frac{1}{4}$ ball for 50mins, then mill with 2 $\frac{1}{2}$ balls for 15mins, to make 4% Dy powder

Figure 3.2 and figure 3.3 shows the differences with high milling energy and low energy milling. To make Dy source powder mixed uniformity with Nd rich powder, powder milling must combine these two milling processes.

3.2 Hot Press Process

After spex milling in an inert atmosphere glove box, the powders were transferred to a cold press in the same glove box without exposure to air. The powders were cold pressed at 30 MPa to a green density of 65%. The rectangular green pellet was 1.3 cm in

width, 1.3 cm in length and about 0.8cm in height.

When transferring the green pellet to the hot press furnace, the pellet was kept in inert atmosphere to protect sample from oxidizing. The pellet was kept in container full of Ar gas. The furnace is pump with Ar gas for over 10mins. Vacuum the hot press furnace right after transferring the sample into furnace.

Hot press is a process application heat and pressure simultaneous. It's a high temperature process to form powder compaction product. [11] Figure 3.4 shows the sketch of hot press process. As the cross area of sample will not change during process, the height change are measured to determine the density variation during process. The uncertainty of height measurement is $\pm 0.05\text{mm}$.

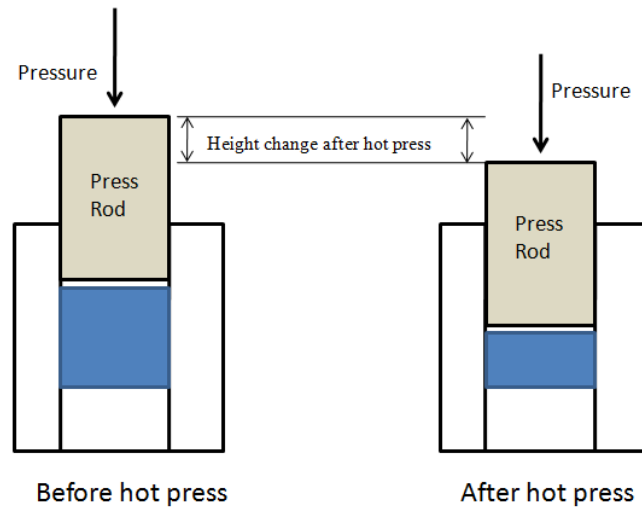


Figure 3.4 hot press process

Figure 3.5, 3.6 and 3.7 are plots of Pressure and Density vs time of three hot press samples. These plots show pressure and density changes as time increase during hot press

process. (Description of samples' labels are in Appendix A).

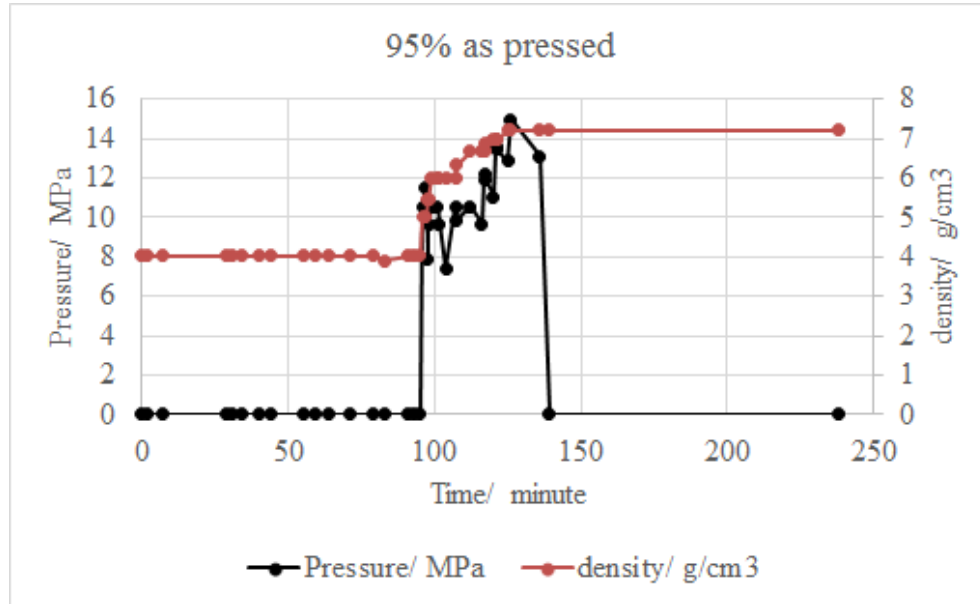


Figure 3.5 95% MTU sample, density and pressure change as time increase

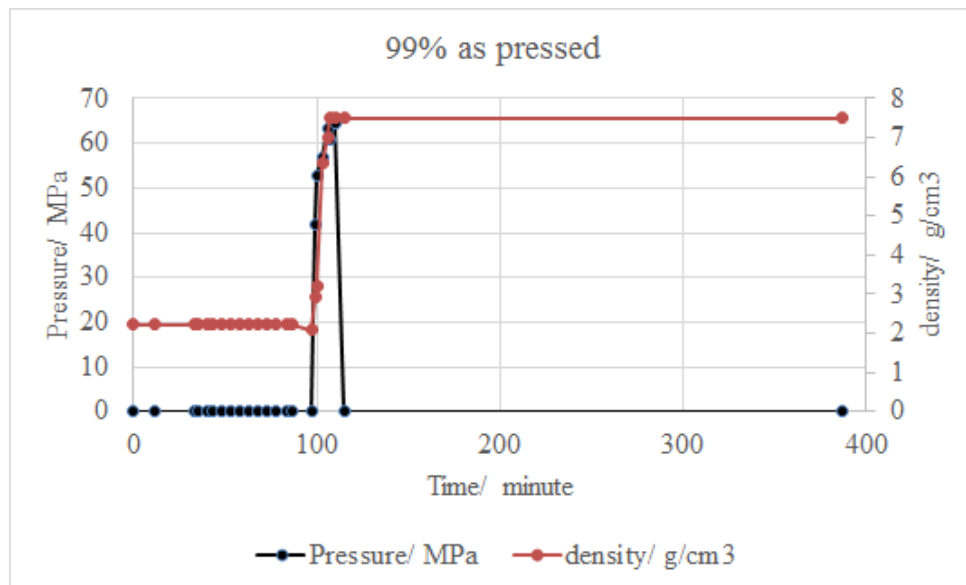


Figure 3.6 99% MTU sample, density and pressure change as time increase

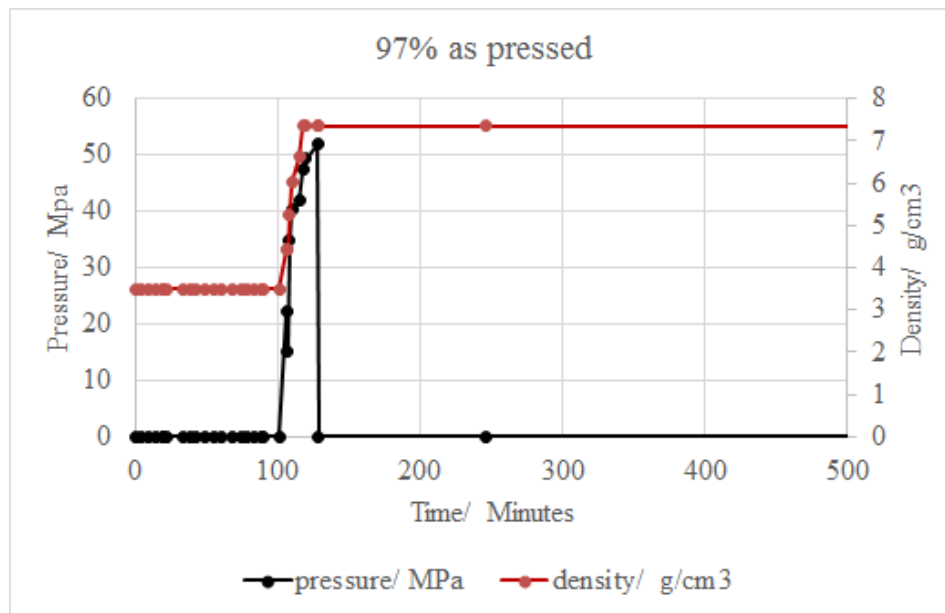


Figure 3.7 97% MTU sample, density and pressure change as time increase

The set point of temperature of hot press process is 850°C. Temperature is increased to 850°C from 0 minutes to 90 minutes, and become stable from 90 minutes to 100 minutes. Application of pressure is by hand and is controlled to be less than 60 MPa to avoid fracture of the sample or die.

3.3 Microstructure Analysis

Obtaining a flat surface for SEM/EDS analysis is complicated by the reactivity of rare earth elements, which have a strong tendency to oxidize when in contact with air or water. [12] During the sample polishing in preparation for SEM analysis, water cannot be used as a lubricant or during surface cleaning. To polish these samples, pieces cut on the slow speed saw are mounted in epoxy for mechanical polishing. The rough polish is done

dry and transitioned from 240 grit to 320 grit and then to 600 grit. Then the sample is cleaned with 99% ethanol and ultrasonic bath. During fine polish of sample, 6 micron and 0.5 micron diamond grit are used for dry polish. Ultrasonically cleaning in 99% ethanol was carried out between each step of the fine polish. After polishing, the samples are stored under inert atmosphere until SEM examination. Just prior to SEM analysis, the sample are coated with Pt-Pd to avoid charging of the epoxy mounted samples.

It was determined that the Nd rich core-Dy rich shell structure of the grains could be directly imaged by using the backscatter detector of the JEOL 6400 SEM provided that high beam currents and long exposure times were utilized. The backscatter contrast was further enhance by processing the images using the gamma function of ImageJ. Colorization based on a greyscale slice was also employed to enhance the higher intensity pixels within the grain corresponding to the local increase in Dy composition. The imaging technique was verified using EDS results. An example of the atomic number contrast and the enhancement of the contrast is shown in figure 3.8.

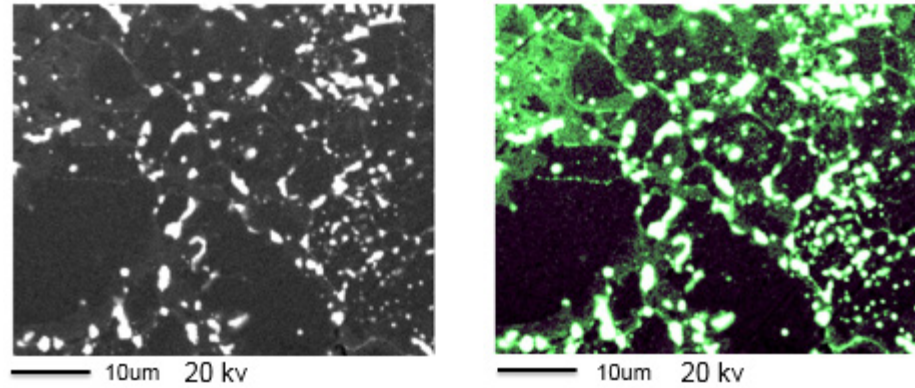


Figure 3.8 MTU hot pressed sample 3B (Appendix A),

Comparison of BSE and BSE pass through a Gamma filter with a grey scale slice colored.

For quantitative analysis sample, EDS and NIST (National Institute of Standards and Technology) are used. EDS are used to collect the spectrum of samples and NIST are used to analysis the content of different elements in the samples. 10 wt% Dy and 0 wt% Dy commercial samples are used as standards for NIST analysis.

3.4 Coefficient of variance*

The analysis of the mixed Dy rich, Dy poor powder samples sintered at various times, temperatures and pressures was carried out by making multiple EDS composition measurements of grain boundary triple junction phase and adjacent grain phase. The coefficient of variance for the Dy grain phase composition measurement was determined using the alloy composition as the average value.

$$\text{Std}^* = \left[\frac{\sum (\text{Dy, center of the grain} - \text{Average of } 50\mu\text{m} \times 50\mu\text{m})^2}{\text{Number of points}} \right]^{\frac{1}{2}} \quad (3.1)$$

$$\text{Coefficient of variance}^* = \frac{\text{Std}^*}{(\text{Average of } 50\mu\text{m} \times 50\mu\text{m})} * 100 \quad (3.2)$$

Dy, center of the grain-----wt% of Dy in the center of grain, test at least 10 grains

Average of $50\mu\text{m} \times 50\mu\text{m}$ ----- average of wt% of Dy in 5 $50\mu\text{m} \times 50\mu\text{m}$ areas

Number of points----- number of center grain points test

The “Std*” in formula is similar to the expression of standard of deviation, the difference is: use Average of $50\mu\text{m} \times 50\mu\text{m}$ substitute the average of the wt% of center of grains.

The "Coefficient of variance*" represents the variance of homogeneous.

As the coefficient of variance defined in this manner measures the deviation of the local Dy composition from the alloy Dy composition, it is used to quantify the degree of Dy homogenization such that a sharply defined core shell structure will correlate to a large coefficient of variance. That is, an Nd rich grain core surrounded by a Dy rich grain shell would be expected to have a large coefficient of variance, while a homogeneous Dy composition throughout the grain will have a small coefficient of variance. A plot of coefficient of variance against sample density is used to demonstrate in a concise manner the general success of processing routes in the development of the core shell

microstructure in dense materials. Figure 4.4 presents the data obtained in this manner for sintered and as hot pressed materials where it is noted that a successful process design for developing the required microstructure will produce a large coefficient of variance at close to theoretical density. It is apparent that the hot press consolidation will allow significant densification while maintaining an inhomogeneous Dy composition.

3.5 Error Analysis

The calculation for error bar of coefficient of variance is based on the error propagation theory.

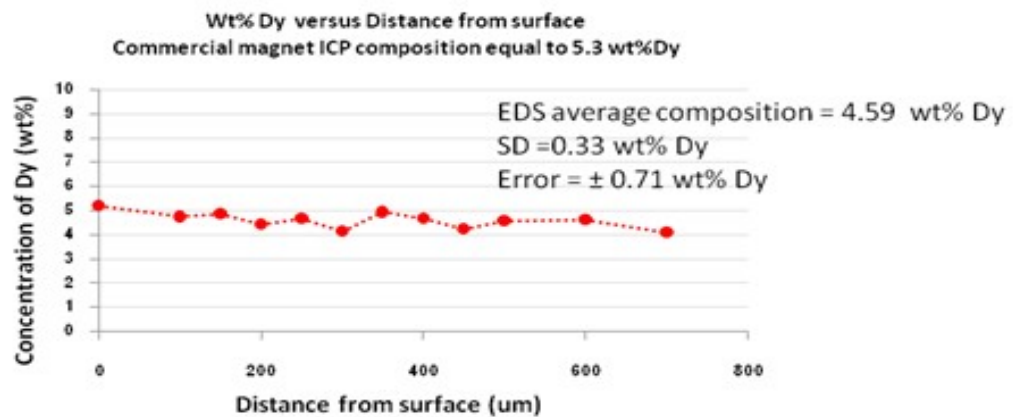


Figure 3.9 Detection error of EDS

Use the formula from [11] to calculate error proporgation.

For uncorrelated variables ($\rho_{AB} = 0$) the covariance terms are also zero,

$$\sigma_{AB} = \rho_{AB}\sigma_A\sigma_B \quad (3.3)[11]$$

In this project, x_1, x_2, \dots, x_n are uncorrelated variables, $\sigma_{AB} = 0$

y_{50} -----50*50 um average data

$$\sigma_{y_{50}} = \frac{\sigma_0}{\sqrt{m}} \quad (3.4)[11]$$

m -----number of 50*50 um data

n -----number of grain center data

σ_0 ----- error comes from SEM detect error, which is 0.71 (Figure 3.9)

To get error propagation of CV, the calculation is based on the formula from [11].

The error of average of 50*50 area data is $\sigma_{y_{50}}$:

y_{50} -----50*50 um average data

$$\sigma_{y_{50}} = \frac{\sigma_0}{\sqrt{m}} \quad (3.5)$$

Error of x_n is σ_0 :

$$\sigma_{x_n} = \sigma_0 \quad (3.6)$$

$$CV = \frac{STD^*}{y_{50}} = \frac{\sqrt{\frac{\sum_1^n (x_n - y_{50})^2}{n}}}{y_{50}} = \sqrt{\frac{\sum_1^n (\frac{x_n}{y_{50}} - 1)^2}{n}} \quad (3.7)$$

Set $f = \sum_1^n \left(\frac{x_n}{y_{50}} - 1 \right)^2$, substitute in (3.7) to get (3.8)

$$\sigma_{CV} = \sqrt{\frac{f}{n} * \frac{\frac{1}{2} * \sigma_f}{f}} = \frac{\frac{1}{2} * \sigma_f}{\sqrt{n * f}} = \frac{\frac{1}{2} * \sigma_f}{\sqrt{n * \sum_1^n \left(\frac{x_n}{y_{50}} - 1 \right)^2}} \quad (3.8)$$

Set $g = \left(\frac{x_n}{y_{50}} - 1 \right)^2$, substitute in f to get (3.9)

$$\sigma_f = \sqrt{\sigma_{g1}^2 + \sigma_{g2}^2 + \dots + \sigma_{gn}^2} \quad (3.9)$$

Set $h = \left(\frac{x_n}{y_{50}} - 1 \right)$, substitute in g to get (3.10)

$$\sigma_g = \frac{h^2 * 2\sigma_h}{h} = 2h * \sigma_h = 2 * \left(\frac{x_n}{y_{50}} - 1\right) * \sigma_h \quad (3.10)$$

From table 3.2, get (3.11)

$$\sigma_h = \frac{x_n}{y_{50}} \sqrt{\left(\frac{\sigma_0}{x_n}\right)^2 + \left(\frac{\sigma_0}{\sqrt{m} * y_{50}}\right)^2} = \sqrt{\left(\frac{\sigma_0}{y_{50}}\right)^2 + \left(\frac{x_n * \sigma_0}{\sqrt{m} * y_{50}^2}\right)^2} \quad (3.11)$$

(3.12) is simplified from (3.11)

$$\sigma_h = \frac{\sigma_0}{y_{50}} \sqrt{1 + \frac{x_n^2}{m * y_{50}^2}} \quad (3.12)$$

Because in this project, $m \geq 5$, and $y_{50} > x_n$, so assume $\sigma_h \approx \frac{\sigma_0}{y_{50}}$,

Put the value of σ_h in (3.10):

$$\sigma_g \approx 2 * \left(\frac{x_n}{y_{50}} - 1\right) * \sigma_h = 2 * \left(\frac{x_n}{y_{50}} - 1\right) * \frac{\sigma_0}{y_{50}} \quad (3.13)$$

Put the value of σ_g in (3.9)

$$\begin{aligned} \sigma_f &= \sqrt{\left(2 * \left(\frac{x_1}{y_{50}} - 1\right) * \frac{\sigma_0}{y_{50}}\right)^2 + \left(2 * \left(\frac{x_2}{y_{50}} - 1\right) * \frac{\sigma_0}{y_{50}}\right)^2 + \dots + \left(2 * \left(\frac{x_n}{y_{50}} - 1\right) * \frac{\sigma_0}{y_{50}}\right)^2} \\ \sigma_f &= \frac{2 * \sigma_0}{y_{50}} \sqrt{\left(\frac{x_1}{y_{50}} - 1\right)^2 + \left(\frac{x_2}{y_{50}} - 1\right)^2 + \dots + \left(\frac{x_n}{y_{50}} - 1\right)^2} \end{aligned} \quad (3.14)$$

Substitute (3.14) into (3.8), get final error (3.15)

$$\begin{aligned} \sigma_{CV} &= \frac{\frac{1}{2}}{\sqrt{n * \sum_{i=1}^n \left(\frac{x_n}{y_{50}} - 1\right)^2}} * \frac{2 * \sigma_0}{y_{50}} \sqrt{\left(\frac{x_1}{y_{50}} - 1\right)^2 + \left(\frac{x_2}{y_{50}} - 1\right)^2 + \dots + \left(\frac{x_n}{y_{50}} - 1\right)^2} \\ \sigma_{CV} &= \frac{\sigma_0}{y_{50} \sqrt{n}} \end{aligned} \quad (3.15)$$

The formula (3.15) can be used to calculate the error of coefficient of variance. The data of experiment matrix with error is shown in Chapter 4.

The density of the hot pressed samples is determined by measuring the dimensions and weight of the rectangular pellet. The uncertainty of measurement of Vernier caliper is $\pm 0.05\text{mm}(\sigma)$.

$$V = a^2 * h, \rho = \frac{m}{V}$$

To calculate the error propagation of density, from formula in [11]

$$\sigma_V = \sigma \sqrt{4 * a^2 h^2 + a^4} \quad (3.16)$$

$$\sigma_\rho = \frac{m * V^{-1} * \sigma_V}{V} = m\sigma * \sqrt{\frac{4 * h^2 + a^2}{a^6 h^4}} \approx \frac{0.05g}{cm^3} \quad (3.17)$$

So the error for relative density: $\sigma_{\%} = 0.7\%$.

The standard error for the slopes is determined as the standard deviation in the CV from that predicted by linear regression, divided by deviation from average of the relative density. The confidence intervals are the standard error multiplied by the critical value at 95% confidence level using the t-score.

Chapter 4 Experiment Results Analysis and Discussion

4.1 Microstructure and Chemistry of Two Alloy Sintered Materials.

Dy composition at the triple junction phase correlated with grain surface enrichment. The presence of a rare earth rich phase at the grain boundary triple junctions in the commercial liquid phase sintered, bulk magnets (LOT3) is demonstrated in figure 4.1 and 4.2

Figure 4.1 showing flat polished surface with EDS overlay of eutectic phase and grain phase.

Dy distribution of GM LOT 3

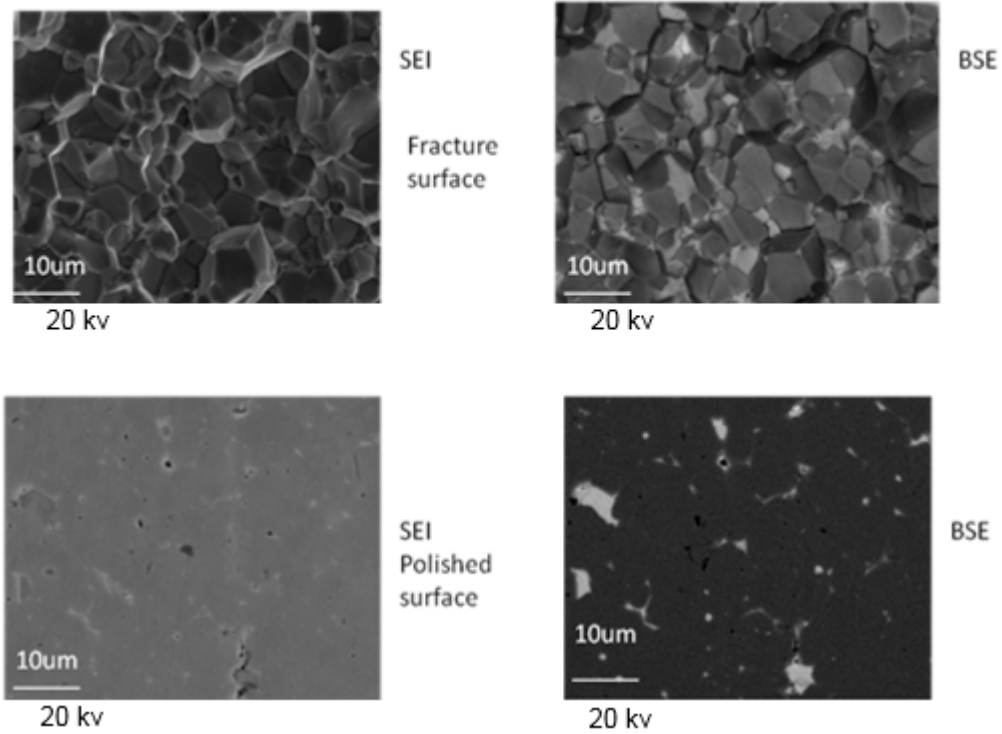


Fig 4.1 (a) SEI/BEI pairs for fractured and flat polished surfaces of commercial bulk magnets (LOT3 Sample from GM)

(ICP: 16.9% Nd, 7.9%Dy, 3.9%Pr, 0.9%B, 0.9%Co, 0.1% Cu)

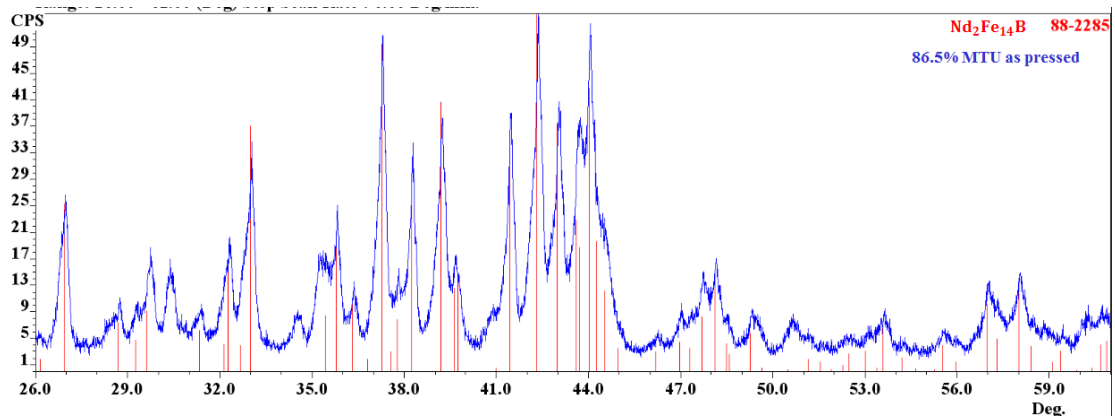


Fig 4.1(b) X-Ray for MTU hot pressed sample compare with $\text{Nd}_2\text{Fe}_{14}\text{B}$ peaks (86.5% MTU as pressed, Appendix A)

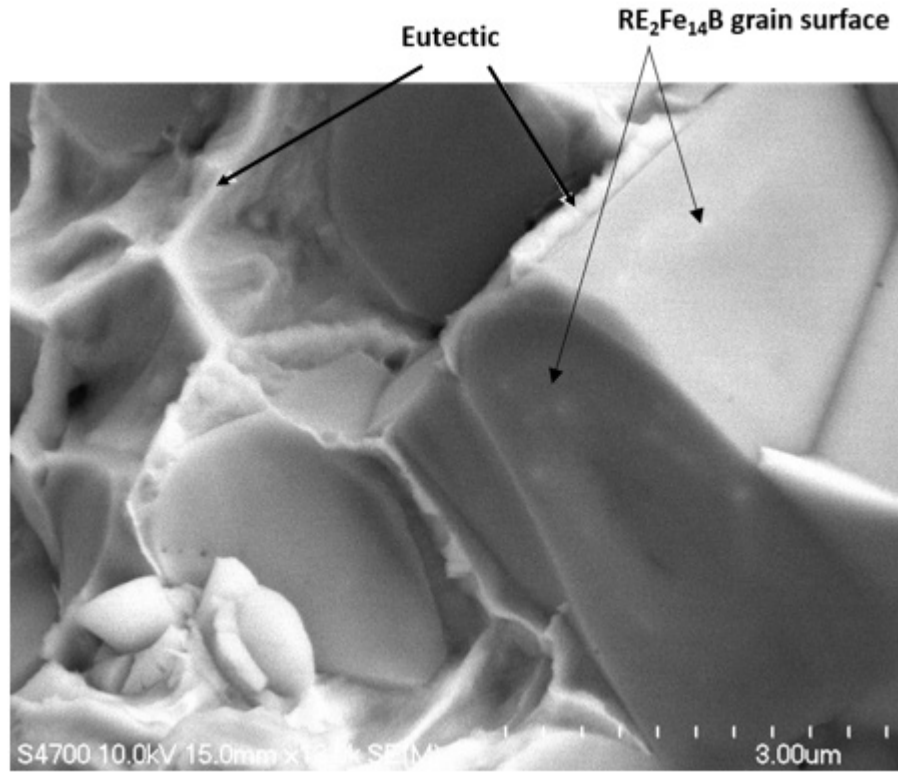


Fig 4.2 Nd, Dy Rich Eutectic micro constituent or solidified eutectic liquid (bright, ductile phase) on grain boundaries and triple junctions (Mixed Dy_{2.34}Fe and Nd_{2.7}Fe₁₄B_{1.4} powder sintered at 950C for 5 hours.)

Hitachi [2] have proposed that an increase in Dy composition of the Eutectic liquid at the grain triple junction via diffusion from the surface will lead to an increase in the Dy composition of the adjacent (Nd)₂Fe₁₄B grain surface, allowing a simple application of SEM/EDS point analysis of the triple junction phase composition and the adjacent grain center as a method to ‘prove’ compositional core-shell development. The approach is necessitated by the difficulty in identifying the exact grain boundary position in flat

polished samples required for quantitative EDS analysis, while identifying the RE rich eutectic liquid remnant is easily done because of the large atomic number contrast. If the basis of the Hitachi analysis is true, then the determination of the triple junction phase composition can be correlated directly to the grain composition at the interface with the eutectic liquid, indicating that compositional core-shell structures can be developed by diffusion through the liquid phase. The Hitachi hypothesis is tested here by examining the ‘tie lines’ between the solidified eutectic liquid and the grain. Standard SEM/EDS are used to measure elemental distributions in the rare earth rich phase at the grain boundary triple junctions (solidified eutectic liquid) and in the grain at 2 microns distance into the grain from the eutectic interface in alloys heat treated for extended periods (15 hours) to test the hypothesis that the grain composition of Dy will increase as the Dy composition of the solidified eutectic liquid increases. Such behavior is required if the measurement of Dy composition at the triple junction phase is to be correlated with grain surface enrichment to produce a core-shell structure. Samples with different Dy content were sintered and heat treated for 15 hours at 950 °C. A plot of the grain composition (at 2 micron distance from the solidified eutectic interface) and Dy liquid composition is shown in figure 4.3.

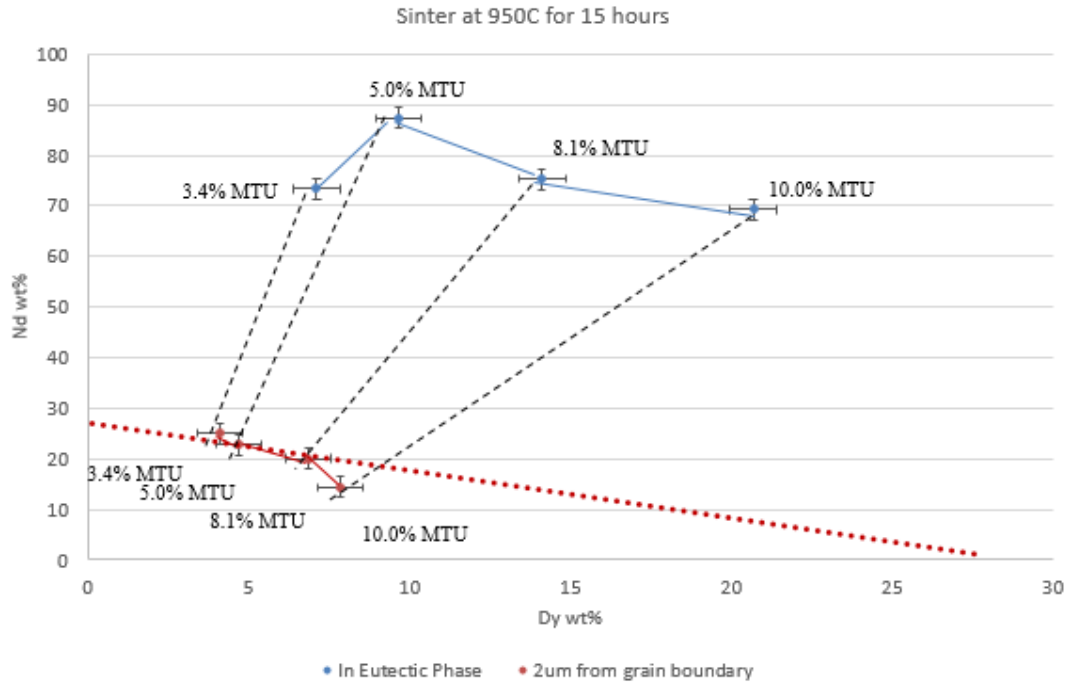


Figure 4.3. The grain composition and Dy liquid composition in samples with different Dy content after sintering at 950°C for 15 hours.

The solid black line in figure 4.3 links the compositions of the triple junction phase in different alloy compositions while the solid red line links the $\text{RE}_2\text{Fe}_{14}\text{B}$ grain compositions for the different alloy compositions. The dotted lines tie the grain composition to the correlated triple junction RE rich solidified eutectic liquid composition. The expected relationship between the Nd wt% and Dy wt% in the stoichiometry $(\text{Nd}_x\text{Dy}_{1-x})_2\text{Fe}_{14}\text{B}$ is shown as the red dashed line. Figure 4.3 demonstration that the triple junction phase (solidified eutectic liquid) Dy composition is correlated with the grain phase Dy composition in that an increase in Dy content in the triple junction ties to an increase in grain composition. It is not known if the dotted lines

will correlate exactly to the tie lines between eutectic liquid and grain composition on the quaternary phase diagram as the eutectic liquid has solidified and possibly undergone a change in composition upon cooling. However, it is apparent in equilibrated samples that the grain composition of Dy will increase as the Dy composition of the solidified eutectic liquid increases, validating the Hitachi method of SEM/EDS analysis used for concluding that compositional core shell structure in $(\text{Nd})_2\text{Fe}_{14}\text{B}$ grains can be formed by boundary diffusion from a Dy source.

4.2 Sintering and Hot Pressing Experiment Matrix

The thesis hypothesis is that hot press consolidation Dy rich powder mixed with Nd rich powder can take place without significant Dy homogenization, allowing for the possibility of compositional core shell grain structure formation. As an examination of this hypothesis, the compositional coefficient of variance (CV) (Equation 3.2) determined by multiple EDS measurements is plotted against the percentage of density, ρ , relative to the theoretical density ρ_{th} in figure 4.4. The consolidation data is augmented by the initial condition that the green density is 65% of theoretical and the CV of the green pellet is 100% by definition.

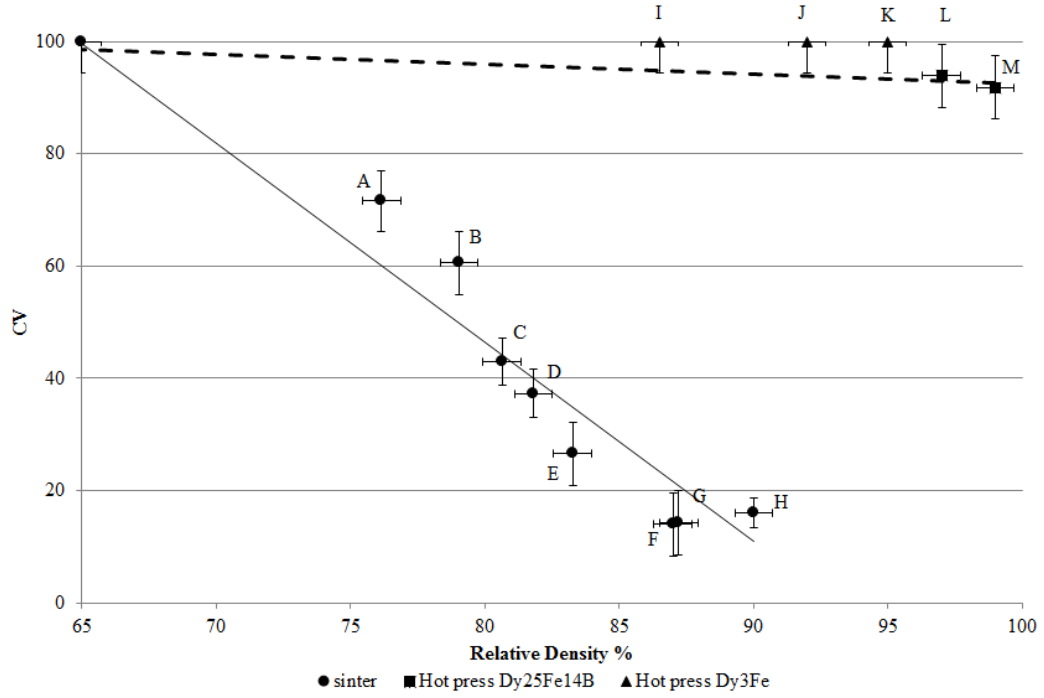


Figure 4.4. Percentage of theoretical density vs coefficient of variance of Dy content.

(Description of sample labels are in Appendix A)

The linear regression ($R^2=0.86$) of the liquid phase sintering coefficient of variance (CV):relative density correlation is:

$$CV = -3.699 \rho/\rho_{th} + 341.29 \quad (4.1)$$

The linear regression ($R^2=0.30$) of the hot pressed samples (CV):relative density correlation is:

$$CV = -0.153 \rho/\rho_{th} + 110 \quad (4.2)$$

A negative slope of large magnitude implies that Dy homogenization is occurring during densification and that sharply defined core-shell microstructure development with sintering process is unlikely, as shown for the liquid phase sintered samples. But the hot

pressed samples demonstrate both high CV and high density, resulting in a regression slope of small negative magnitude. Figure 4.4 then suggests the possibility that a compositional core-shell microstructure may be produced using the hot pressing processing route. Because of this physical relevance, the linear regression slopes will be referred to as core-shell slopes. As core-shell slope is the physically relevant parameter in comparing the propensity of the two processes to form compositional core-shell structures and is critical to corroboration of the hypothesis, it is necessary to confirm that the difference between sintering and hot pressing CV: relative density slopes is statistically significant. To this end, the standard errors of the core-shell slopes were determined, which were then multiplied by the critical value at 95% confidence level (using the t-score) to specify the 95% confidence intervals of the core shell slope values. Table 4.2 shows the relevant statistical consideration of the two slopes in figure 4.4. It is apparent that 95% confidence intervals of the core-shell slopes for the two processes do not overlap, providing a high statistical confidence that the hot press processing approach produces a composition variation at high density that is significantly more inhomogeneous than the two alloy liquid phase sinter process. This result provides corroboration for the hypothesis of the thesis.

Table 4.1 Statistical analysis of the hot press and sinter core-shell slopes in figure 4.4

Process	Core-Shell Slope	Standard Error	95% Confidence Interval
Liquid phase Sintered	-3.70	0.69	-3.01 to -4.39
Hot Press	-0.15	0.14	+0.23 to -0.53

Table 4.1 showing the hot press core shell slope is significantly less negative than the sinter core-shell slope.

Figure 4.4 is an indirect measure of the spatial Dy composition data but is nevertheless useful for a semi-quantitative analysis of process kinetics (section 4.4). In section 4.3, direct imaging of the Dy poor core-Dy rich shell microstructure using backscatter electron imaging and element mapping EDS images is presented together with EDS measurements of Dy spatial variation.

4.3 Microstructural Evidence of Dy Composition Core Shell Structure

The presence of a Dy enriched shell on the boundaries of the $(\text{Nd})_2\text{Fe}_{14}\text{B}$ grains was found to produce sufficient atomic number contrast in backscatter images to allow direct imaging of the Dy composition enhancement due to the formation of

$(\text{Dy}_x\text{Nd}_{1-x})_2\text{Fe}_{14}\text{B}$ alloy as the atomic number of Dy is 66 and Nd is 60. A series backscatter SEM images collected under high signal to noise conditions and associated EDS results of the hot pressed microstructures are shown in figure 4.5 (a) (b) (c).

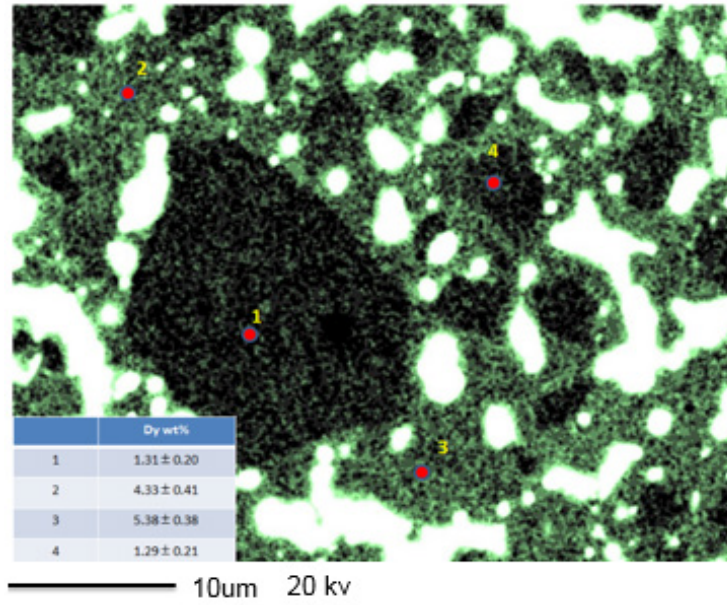


Figure 4.5 (a) MTU 3A

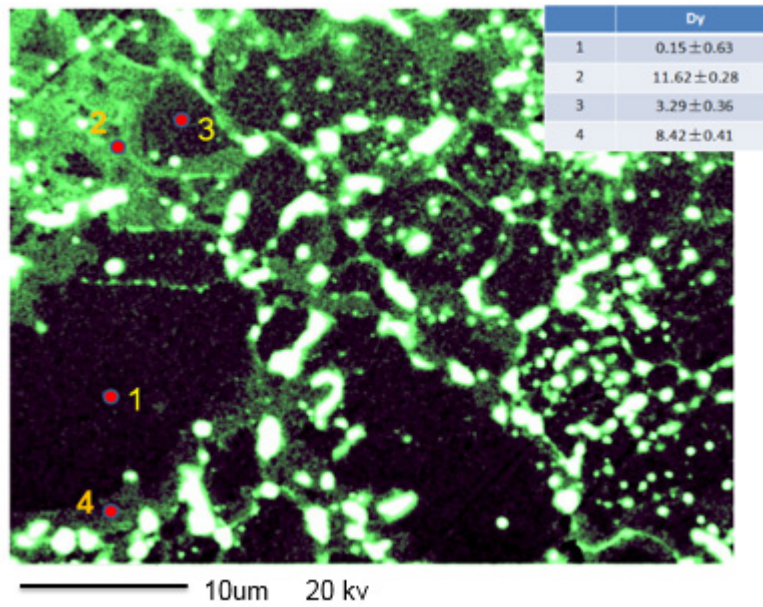


Figure 4.5 (b) MTU 3B

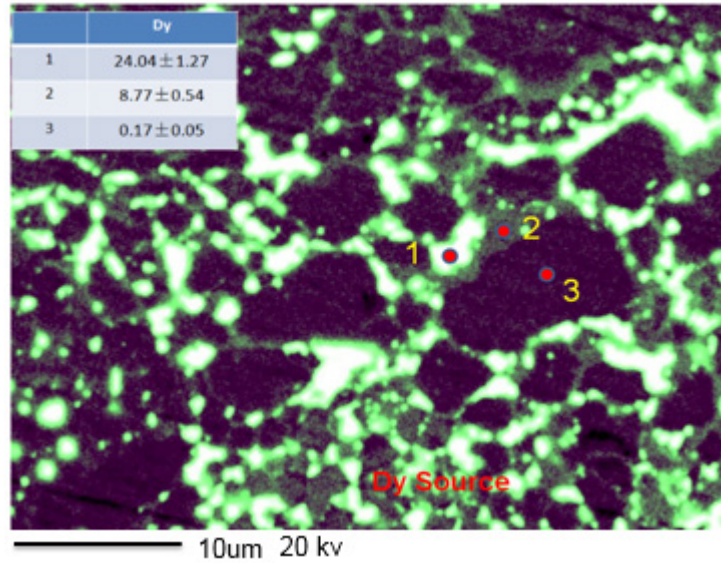


Figure 4.5 (c) MTU 3C

Figure 4.5 (a) MTU 3A, High energy milling of NdFeB ingot with Dy source for 15 minutes. 2 hours at 850C under pressure.

Figure 4.5 (b) MTU 3B, High energy milling of NdFeB ingot for 15 minutes with Dy source at last 5 minutes. 2 hours at 850C under pressure.

Figure 4.5 (c) MTU 3C, High energy milling of NdFeB ingot for 15 minutes with Dy source at last 5 minutes. 40 minutes at 850C under pressure.

The brightest areas in the image correspond to the eutectic liquid at the grain triple junctions. The grain boundary regions connection the triple junctions can be seen as having a higher backscatter intensity than the grain centers, suggesting an enrichment in the Dy content. These are the Dy rich shells. The increase in Dy at the high intensity backscatter regions of the grain and grain boundary are verified using EDS where the EDS results are shown in the table inset in the images.

The backscatter images of the hot press core-shell structures are directly compared to the core shell microstructure developed by the Hitachi process in a magnet obtained from the electric motor of a commercial hybrid vehicle (Honda Prius) (figures 4.6).

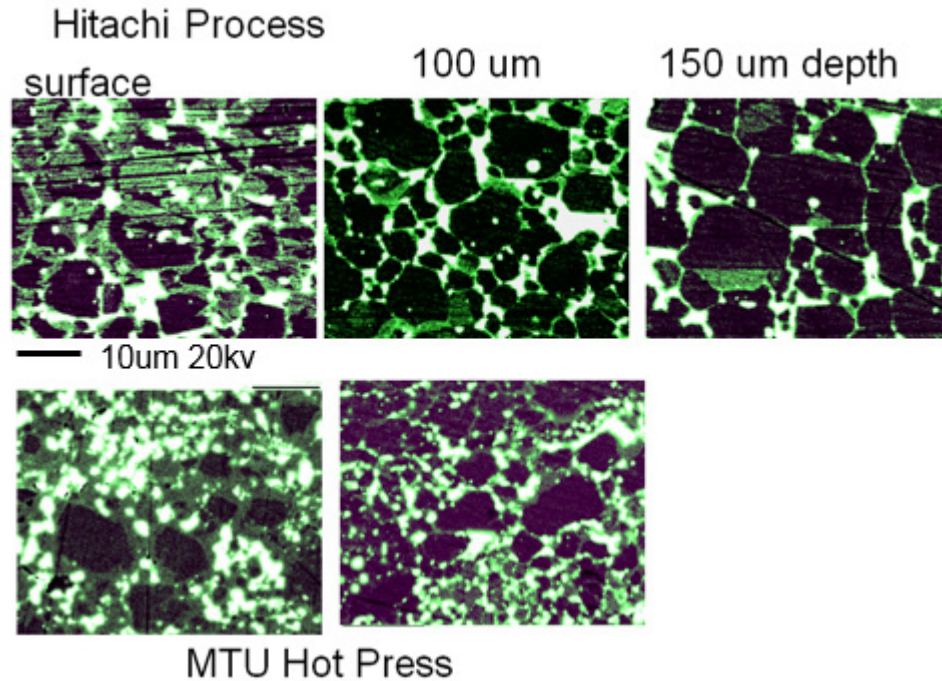


Figure 4.6 Comparison of MTU 3C hot pressed sample and commercial magnet from the electric motor in a Honda Prius.

Although there are clear differences in grain size between the commercial magnet and the hot press material, the backscatter images reveal the Dy enriched core shell microstructure are evident in both cases. Areas of the hot press samples close to the Dy source have a similar appearance to the surface of the Hitachi process grain boundary diffused magnets (left hand side of figure 4.6) while areas further from the Dy source points in the hot press samples appear similar to Hitachi process areas approximately 100

um from the surface diffusion source.

A similar approach to revealing the Dy enriched core-shell microstructure is utilized in chemical mapping of the microstructure, where the strength of the Dy EDS signal is correlated to positions on a flat polished cross section producing an image which shows qualitatively spatial variation of the Dy composition. Images using this technique are shown in figures 4.7.

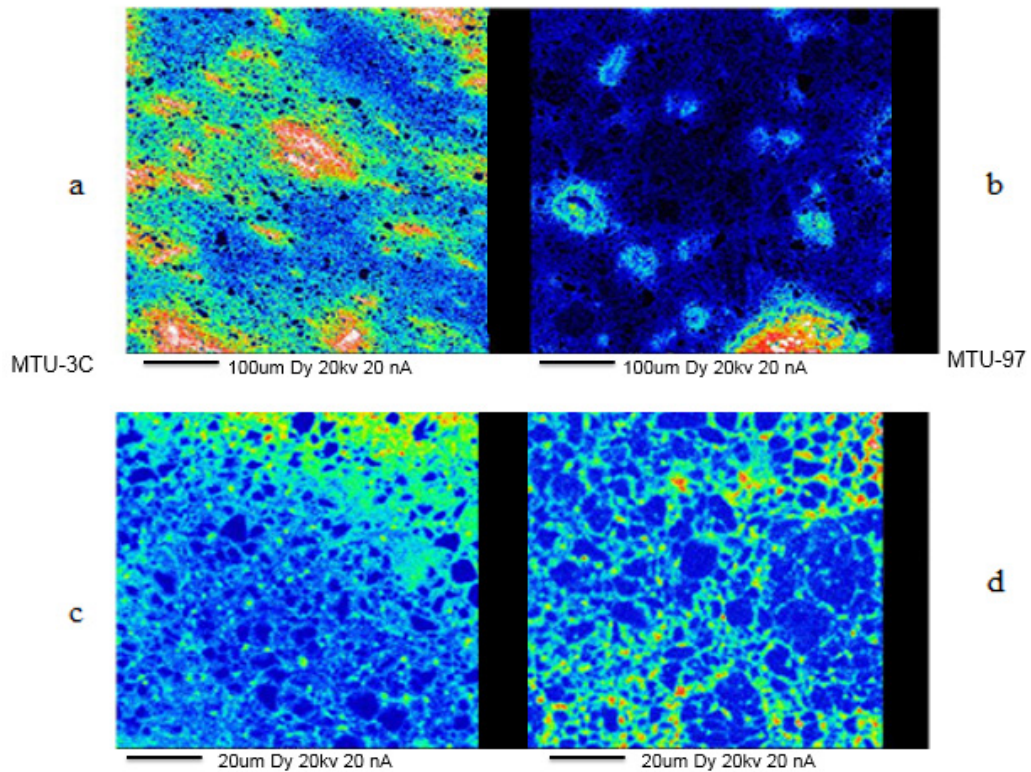


Figure 4.7 Electron Microprobe EDS Dy distribution map for MTU samples showing Dy localization on the grain boundaries (obtained by Wakade and Waldo, GM)

Figure 4.7 (a), (b) two lower magnification images in figure 4.7 showing regions

corresponding to the Dy rich powder sources (orange to white) surrounded by grains with Dy composition core shell structure.

Figure 4.7 (c), (d) two higher magnification images in figure 4.7 showing grains with Dy composition core shell structure.

In figure 4.7, the concentration of Dy (based on the relative strength of the Dy EDS) is correlated to the color scale on the right hand side of the image. The color scales on the images color are slightly different, but in general, black in 4.7 a,b corresponds to $(\text{Nd})_2\text{Fe}_{14}\text{B}$ while dark blue in 4.7 c,d corresponds to $(\text{Nd})_2\text{Fe}_{14}\text{B}$. The lighter blue to green to yellow to orange to white are in increasing order of Dy composition it means Dy composition is higher. Figure 4.7 (a) (b) reveal that there is substantial local Dy composition enrichment with cross sections approaching 10^{-8} m^2 . These large (relative to grain size) Dy rich regions are proposed to be the remnants of the Dy rich powder ($\text{Dy}_{25}\text{Fe}_{14}\text{B}$) that was originally mixed with the Nd rich powder. These large Dy rich regions appear as the sources for Dy distribution onto the boundaries of the $(\text{Nd})_2\text{Fe}_{14}\text{B}$ grains, as revealed in the higher magnification images in figures 4.7 (c) (d) with an expanded color scale. Figures 4.7 (c) (d) can be qualitatively compared with the backscatter images in Figure 4.5. Both Figure 4.7 and 4.5 are indicative of compositional core shell structures. As in figures 4.6 and 4.7, direct comparison can again be made between the imaging of hot press core shell composition structures and the imaging of

core shell composition structures Hitachi process samples from the Prius electric motor.

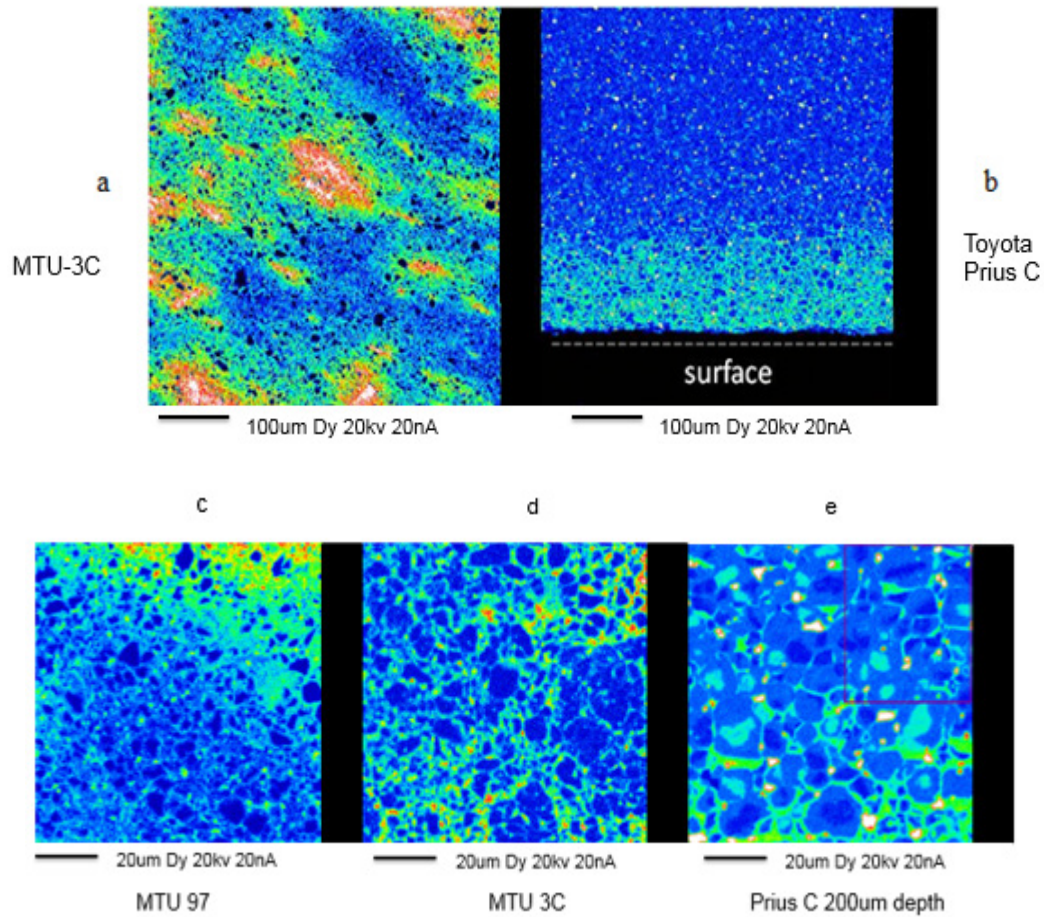


Figure 4.8 Electron Microprobe EDS Dy distribution map for Toyota Prius C magnet and MTU samples showing Dy localization on the grain boundaries (obtained by Wakade and Waldo, GM)

Figure 4.8 (a) (b) Low magnification chemical mapping image of an MTU hot press sample compared to the low magnification chemical mapping image of a Hitachi process sample.

Figure 4.8 (c) (d) (e) Higher magnification images comparing the chemical mapping

images of MTU hot press sample and a Hitachi process samples at 200 um depth.

The EDS Dy mapping images are qualitatively consistent with the backscatter images, which are also backed up by quantitative EDS measurements on local Dy concentrations. Both the backscatter images and Dy element mapping images of the core-shell structure in the hot press samples are consistent with the description of a large coefficient of variance for these materials which reveal the goal structure: Dy enriched shell structure on the boundaries of $(\text{Nd})_2\text{Fe}_{14}\text{B}$.

Figures 4.4-4.8 provide visual evidence that the hot press consolidation of Nd rich powder mixed with Dy rich powder can deliver a high density material with Dy localized at the grain boundary. The goal of the Hitachi process would then seem to be met using the mixed powder approach under hot press consolidation. However, there is a significant difference that should be noted. By reference to figure 4.8, it is noted that the grain boundary enrichment from the Hitachi process that can be observed by EPMA mapping occurs mainly within 200 um of the surface. This is simply a limitation of long range diffusion in that a concentration gradient is required to drive diffusion from the surface source into the bulk magnet and this concentration gradient will be continually reduced as the Hitachi process extends in time. In the case of the mixed powder, the Dy sources are distributed throughout the bulk of the material, including the surface region. The contrast between the Hitachi process and the GM process is that the volume of the magnet effected by grain boundary enrichment of Dy is much greater in the GM process.

This demonstration of the core-shell microstructure development is further tested using quantitative EDS to measure how the Dy composition varies across the sample, particularly as distance increases from the Dy source. Backscatter imaging can be used to identify a local Dy ‘source’ present at locations in the sample which is supposed to correspond with a Dy rich particle in the original mixed powder. As shown in figure 4.9. The Dy composition is measured (using EDS) as a function of distance from this powder particle in both the grain and in the eutectic.

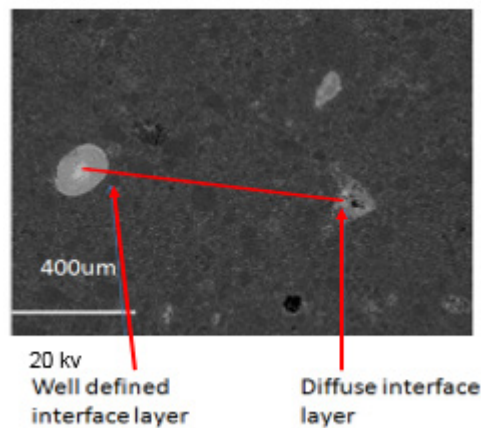


Figure 4.9 Low magnification of the hot press microstructure of mixed Dy rich and Nd rich powder. EDS of Dy composition is undertaken along the red line between two Dy sources. (MTU 95% as pressed sample)

Figure 4.10, 4.11 and 4.12 examine the Dy composition in the triple junction eutectic liquid and adjacent grain composition as a function of distance from the Dy source in

three different hot press samples. MTU 97% (hot pressed, and density 97%), MTU 95% (hot pressed, and density is 95%) and MTU 99% (hot pressed, and density 99%) as pressed samples are in Appendix A. This is effectively a post-mortem analysis of the Dy transport through the liquid phase and solid phase during Dy diffusion between Dy sources. Referring to Figure 2.4, the technique applied here is similar to the technique utilized by Hitachi in their patent [2] to produce evidence that the diffusion from the surface resulted in a core shell structure. The technique is reproduced here to show that the hot pressing of mixed Nd rich and Dy rich powders can produce the same type of result trumpeted by Hitachi as the experimental verification of compositional core-shell microstructure development. In the figures 4.10-4.12, all show the result that the eutectic at the grain triple junction has a measurable Dy composition decreasing from the source Dy composition, while the Dy composition adjacent to the triple junction eutectic (~2 um) within the grain becomes vanishingly small as the distance from the source increases. The EDS results thus demonstrate the same behavior reported in the Hitachi patent [2] that was used to ‘prove’ the concept of compositional core shell microstructure.

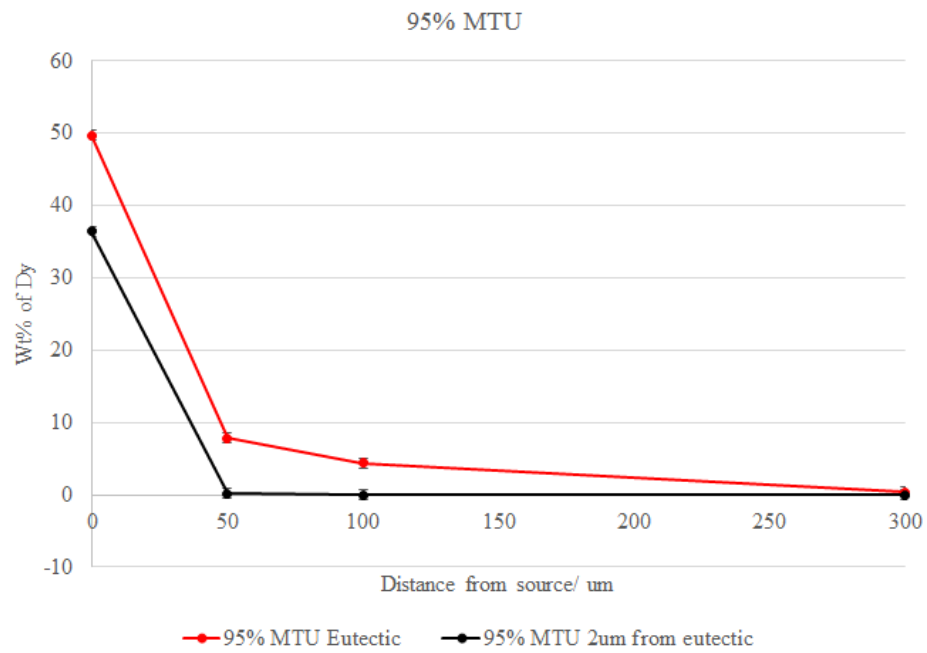


Figure 4.10 Dy diffusion in hot pressed MTU 95% sample

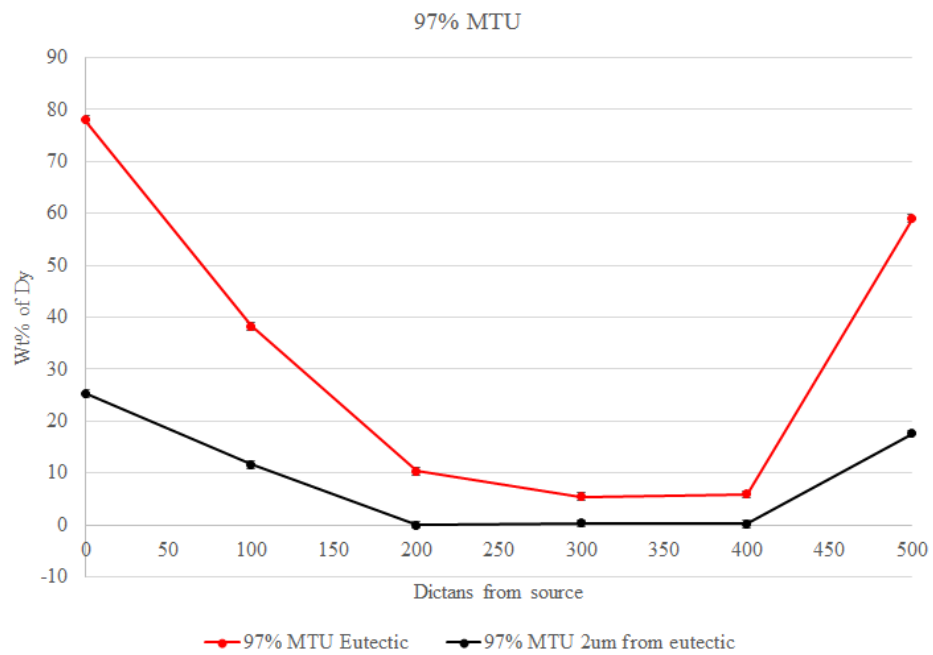


Figure 4.11 Dy diffusion in hot pressed MTU 97% sample

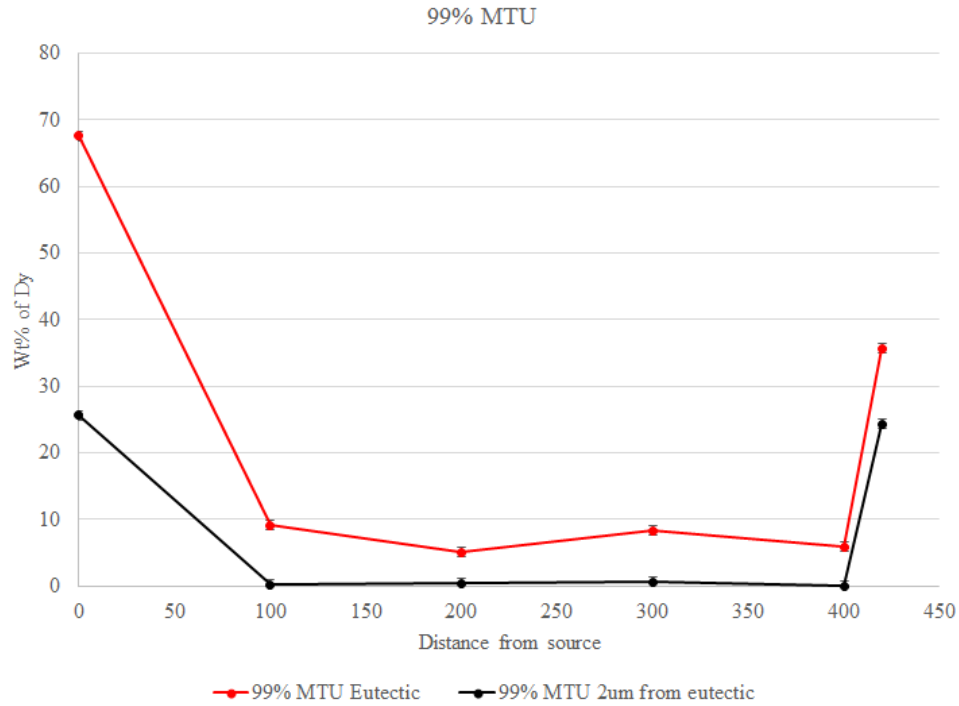


Figure 4.12 Dy diffusion in hot pressed MTU 99% sample

4.4 Analysis and Discussion of Results.

The hypothesis examined in this work is that if hot pressing is used to consolidate mixed Dy rich and Nd rich powders, then a core-shell composition structure can be produced because the rate of consolidation is enhanced relative to the composition homogenization rate. The previous section has indeed demonstrated core-shell composition structures using three independent methods. However, a simple quantitative analysis may allow a more in depth understanding of the underlying principles. To develop such an approach, the compositional homogenization is correlated with a solution to the 1 dimensional diffusion equation

$$C = C_{Ave} * \left[1 + \cos\left(\frac{2\pi x}{L}\right) * \exp\left[-\left(\frac{2\pi}{L}\right)^2 D t\right] \right] \quad (4.3a)$$

In equation 4.3a, C is the composition of Dy, C_{Ave} is the average composition of Dy, D is diffusion coefficient, L is a characteristic diffusion length and t is time.

Equation (4.3b) can be written in a form consistent with the concept of a compositional coefficient of variance, consistent with the boundary conditions as $CV/100=1$, $t=0$ and $CV/100=0$ when $t=\infty$.

$$\frac{C_{Max}-C_{Ave}}{C_{Ave}} = \frac{CV}{100} = \left[\exp\left[-\left(\frac{2\pi}{L}\right)^2 D t\right] \right] \quad (4.3b)$$

The consolidation rate has been modeled using the expression

$$\frac{d}{dt} \rho * \frac{1}{\rho} = \frac{H * D * \Omega * \Phi^m * (\Sigma + P_{applied})}{G^n * k * T} \quad (4.4)[13]$$

In equation 4.4, ρ is density, H is constant, D is diffusion coefficient, Ω is atomic volume, Φ is the stress intensification factor, $m=2$ for grain boundary diffusion and $m=1.5$ for volume diffusion. $P_{applied}$ is the applied pressure. Σ is the sintering stress. G is grain size, $n=2m-1$, k is Boltzmann's constant and T is temperature.

The sintering stress has been approximated as

$$\Sigma = 2 * \frac{\gamma_{gb}}{G} + 2 * \frac{\gamma}{r} \quad (4.5)[14]$$

In equation 4.5, γ_{gb} is interfacial energy of grain boundary, γ is interfacial energy of pore and r is the radius of a pore.

For systems with non-uniform particle sizes, the grain size, G, will coarsen during consolidation, thus the diffusion length and sintering stress for consolidation is a complex function of time as represented in equation (4.6)

$$\frac{d}{dt} \rho * \frac{1}{\rho} = \frac{H * D * \Omega * \Phi_{(t)}^m * (\Sigma_{(t)} + P_{\text{applied}})}{k * T * G_{(t)}^n} \quad (4.6)$$

Or in the form of a general solution to the differential equation 4.6

$$\frac{\rho}{\rho_{\text{th}}} = \frac{\rho_0}{\rho_{\text{th}}} * \exp \left(\frac{H * D * \Omega}{k * T} * \int_0^t \frac{\Phi_{(\tau)}^m * (\Sigma_{(\tau)} + P_{\text{applied}})}{G_{(\tau)}^n} d\tau \right) \quad (4.7)$$

Equation 4.7 is similar to the ‘Master Sintering Curve’ [15] with the microstructure parameters integrated over time rather than over density. Park et [16] and Randall [17] have applied the Master Sintering Curve (equation 4.7) for both liquid phase sintering and solid state sintering and have proposed it valid for both processes.

When the initial conditions of the green pellet include non-uniform grain/particle and pore sizes, the consolidation rate is known to follow a semi-log law. [18]

Such a semi-log law can be approximated by an exponential function such that

$$\frac{\rho_0}{\rho_{\text{th}}} * \exp \left(\frac{H * D * \Omega}{k * T} * \int_0^t \frac{\Phi_{(\tau)}^m * \Sigma_{(\tau)}}{G_{(\tau)}^n} d\tau \right) = 1 - \frac{\rho_{\text{th}} - \rho_0}{\rho_{\text{th}}} * \exp \left(- \frac{H * D * \Omega * \Psi}{k * T} * t \right) \quad (4.7a)$$

Substitute into equation (4.7)

$$\frac{\rho}{\rho_{\text{th}}} = 1 - \frac{\rho_{\text{th}} - \rho_0}{\rho_{\text{th}}} * \exp \left(- \frac{H * D * \Omega * \Psi}{k * T} * t \right) \quad (4.8a)$$

Where Ψ encompasses the effective sintering stress and diffusion geometry with units Pa/m^2 . ρ is density, ρ_{th} is theoretical density. The form of Ψ from this analysis is described in appendix B as

$$\frac{\rho_0 * \frac{\Phi_{(0)}^m * \Sigma_{(0)}}{G_{(0)}^n}}{(\rho_{\text{th}} - \rho_0)} = \Psi \quad (4.8b)$$

for liquid phase sintering and

$$\frac{\rho_0 * \frac{\Phi(o)^m(\Sigma(o)+P_{\text{applied}})}{G(o)^n}}{(\rho_{\text{th}} - \rho_0)} = \Psi \quad (4.8c)$$

for hot pressing.

The linearization of equation 4.3 is

$$\frac{C_{\text{Max}} - C_{\text{Ave}}}{C_{\text{Ave}}} = \frac{CV}{100} = 1 - \frac{4 * \pi^2 * D * t}{L^2} \quad (4.9)$$

The linearization of equation 4.8(a) is

$$\begin{aligned} \frac{\rho}{\rho_{\text{th}}} &= 1 - a * \left(1 - \frac{H * D * \Omega * \Psi}{k * T} * t \right) = \frac{H * D * a * \Omega * \Psi}{k * T} t \\ a &= \frac{\rho_{\text{th}} - \rho_0}{\rho_{\text{th}}} \end{aligned} \quad (4.10)$$

Taking the ratio of the time derivatives of equations 4.9 and 4.10 determine an expression that describes the slope of the linear regressions in figure 4.5.

$$\frac{\frac{d}{dt} CV}{\frac{d(\frac{\rho}{\rho_{\text{th}}})}{dt}} = \frac{d}{d(\frac{\rho}{\rho_{\text{th}}})} CV = \frac{-\frac{4 * \pi^2 * D_h}{L^2}}{\frac{D_c * a * \Omega * \Psi}{k * T}} = -\frac{4 * \pi^2 * D_h * k * T}{D_c * a * \Omega * \Psi * L^2} \quad (4.11)$$

Where the diffusion coefficient for homogenization, D_h , has been distinguished from the diffusion coefficient for consolidation, D_c .

4.5 Determination of Mechanism Activation Energies

From the double natural log of equation 4.10,

$$-\ln \left(\ln \left(\frac{\rho}{\rho_0} \right) \right) + \ln \left(\frac{1}{T} \right) = \frac{Q_c}{k * T} - \ln \left(\frac{H * D_0 * F(t) * \Omega}{k} \right) \quad (4.12)$$

Where the diffusion coefficient for consolidation, D_c , has been described using

$$D_c = D_0 * \exp \left[\left(\frac{-Q_c}{k} \right) * \frac{1}{T} \right]$$

Similarly, for the coefficient of variance, equation a1 may be manipulated to give

$$-\ln(-\ln(CV)) = -\ln\left(\frac{4*\pi^2*t}{L^2} * D_0\right) + \frac{Q_h}{k*T} \quad (4.13)$$

Where the diffusion coefficient for compositional homogenization is given as

$$D_h = D_0 * \exp\left[\left(\frac{-Q_h}{k}\right) * \frac{1}{T}\right]$$

The values on the lhs of equations (4.12 and 4.13) are known and can be plotted versus 1/T as in figure 4.13 and 4.14, and analyzed by linear regression. The coefficient of determination for the linear correlation of the consolidation and homogenization temperature dependence is ($R^2=0.947$) and ($R^2=0.863$) respectively. The slopes of the lines are then the normalized activation energy for consolidation, $Q_c/k= 2400.1 \text{ K}^{-1}$ (20 kJ/mol), and for composition homogenization $Q_h/k= 4425.4 \text{ K}^{-1}$ (39 kJ/mol). These activation energies are much less than the proposed activation energy for solid state diffusion of Dy in Nd₂Fe₁₄B (315 kJ/mole [19]). However, the activation energy for diffusion in molten (liquid) metal, which follows the approximate correlation of $Q_{\text{Liquid}} \approx 3.2 R T_{\text{melt}}$ [20] are an order of magnitude smaller than that found for solid state diffusion. A comparison of the activation energies determined from figures 4.13 and 4.14, and other liquid phase sintering systems with transient liquid phase behaviors is displayed in table 4.2.

Table 4.2 Comparison of the activation energies to the melting point correlation.

Chemistry	Qc ,Densification Activation Energy, kJ/mol	Qc/(3.2 R T _{melt})
Fe-Nd-Dy-B [MTU]	20	0.79
W-Fe-Ni [16]	79	1.73
Ti-Al [21]	90	2.53

The low activation energies are suggestive of dissolution and reprecipitation through transport in the liquid phase as a primary mechanism of consolidation [16] Because the activation energy for composition homogenization is also quite low compared to solid state diffusion, the possibility must be considered that dissolution reprecipitation by liquid phase transport is also a mechanism of action for reduction in CV during consolidation. In this case, formation of $Dy_xNd_{2-x}Fe_{14}B$ alloy could occur by dissolution of $Nd_2Fe_{14}B$ into the Dy rich liquid coincident with the reprecipitation of the alloy composition in equilibrium with the liquid phase. A dissolution-reprecipitation process driven by composition inhomogeneity has been described in other liquid phase sintering processes where the liquid is not initially in equilibrium with the solid. [22, 23] The low activation energy for composition homogenization would also seem to be consistent with the rapid decrease in CV with density, resulting in the necessity of using pressure assisted sintering to reduce the time and temperature required for consolidation in an attempt to form the Dy rich shell-Nd rich core microstructure.

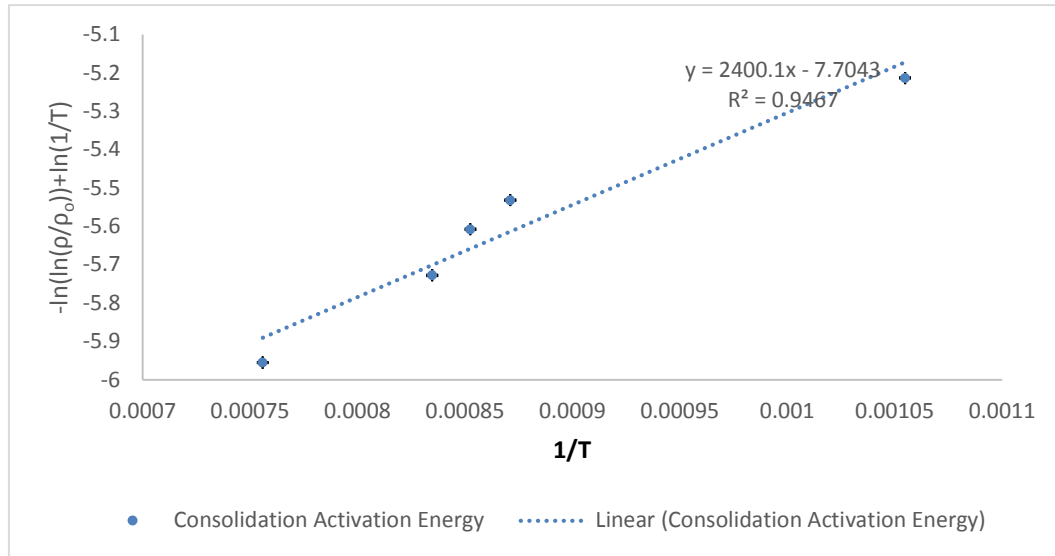


Figure 4.13 Determination of activation energy for consolidation diffusivity

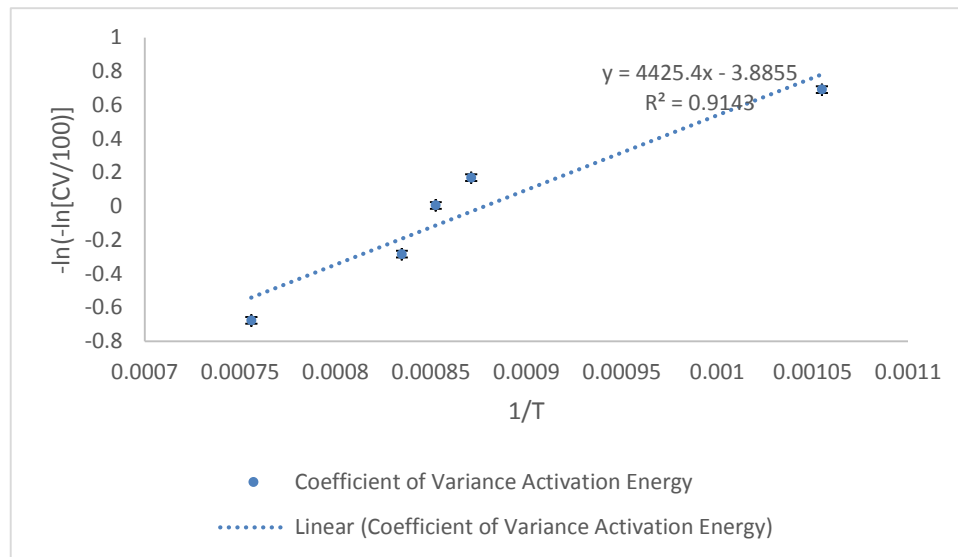


Figure 4.14 Determination of activation energy for homogenization diffusivity.

4.6 Analysis of Hypothesis

The coefficient of variance (CV) is plotted against the relative density in figure 4.4 of

the last chapter. Although this reveals a great deal about the observed experimental behavior, the temperature is a variable in equation 4.11, that is not accounted for in examining the slopes of the sinter and hot press linear regression. Here, an attempt is made to be more quantitative by examining the role of temperature in the CV vs relative density behavior, which was collected at a range of temperatures. Appendix A Process temperature, CV and density of experiment matrix.

The temperature variable may be accounted for by plotting $\frac{\rho}{\rho_{th}} * \frac{T \cdot k}{\Omega} * \exp(\frac{Q_c - Q_h}{k \cdot T})$ against CV/100, where Q_c and Q_h are the activation energies for consolidation and homogenization diffusivity respectively.

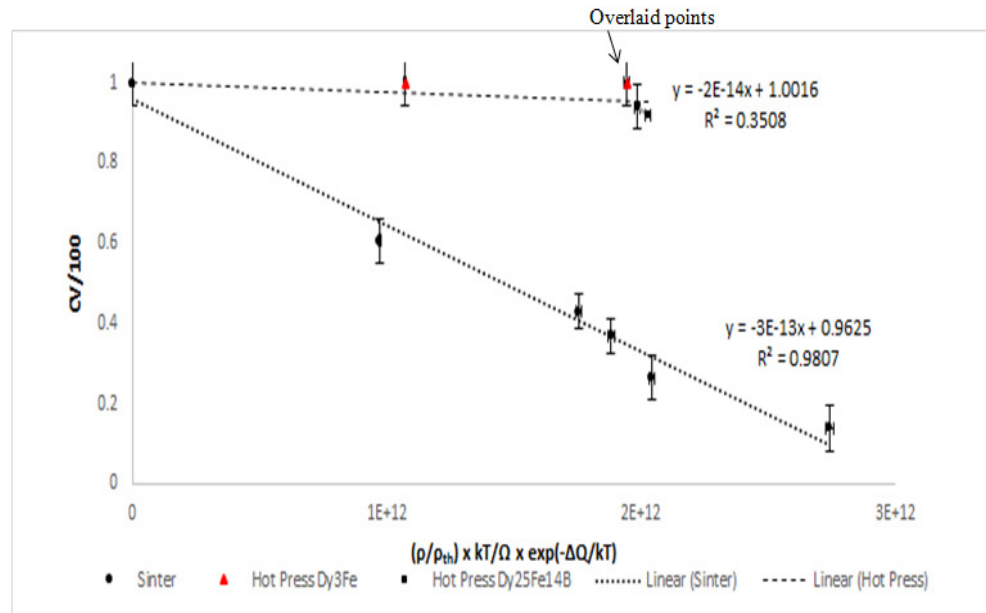


Figure 4.15 core shell slope of sintering and hot press sample. As marked, one Hot press Dy₃Fe point and one Hot press Dy₂₅Fe₁₄B points are overlaid.

The experimental data for the CV and relative density are augmented with a data

point developed by projected behavior that at T=0 K, the CV will be 1 (100%). That is, at absolute zero, the x-axis is at the origin by definition and homogenization processes that could reduce CV are null. The slope for the hot press samples ($-2 * 10^{-14} \text{ m}^3 \text{ J}^{-1}$) is found to be approximately an order of magnitude greater (less negative) than that for the free sinter samples ($-3 * 10^{-13} \text{ m}^3 \text{ J}^{-1}$) with the standard error in the slopes determined as $9.9 * 10^{-15} \text{ m}^3 \text{ J}^{-1}$ and $9.7 * 10^{-15} \text{ m}^3 \text{ J}^{-1}$ respectively. As it is proposed that the slopes in the temperature adjusted plot (figure 4.15) correlate with the development of a composition core-shell structure, the slopes will be referred to as core-shell slopes, with the less negative the slope, the more likely core-shell composition structures are formed. The analytical form for the core-shell slope ratio for the temperature adjusted data that can be compared to the experimental result is

$$\frac{\frac{4*\pi^2}{a*\Psi_{\text{HotPress}}*L^2}}{\frac{4*\pi^2}{a*\Psi_{\text{Sinter}}*L^2}} = \frac{2*10^{-14}}{3*10^{-13}} = 0.067 \pm 0.033 \quad (4.12)$$

Assuming the diffusion geometry and lengths (G and L) are similar between the sinter and hot press samples, then equation 4.12 simplifies to a relationship between the experimentally determined core-shell slope ratio and the model prediction of the slope ratio as

$$\frac{\Psi_{\text{Sinter}}}{\Psi_{\text{HotPress}}} = \frac{\Sigma}{\Sigma + P_{\text{applied}}} = (0.067 \pm 0.033)_{\text{Experimental}} \quad (4.13)$$

The smaller this ‘core-shell’ slope ratio, the greater the effect of applied pressure on allowing compositional core-shell grain structure development during consolidation. The

validity of the model can be examined by comparison with literature values of the sintering stress for micron scale particles. The sintering stress Σ is generally expected to be 0.5 to 3 MPa [25 and Appendix B], while the applied pressure is on the order of 30-60 MPa. This suggests that there is a range of core-shell slope ratios to be expected from theory shown in equation 4.14.

$$0.008 < \left(\frac{\Sigma}{\Sigma + P_{\text{applied}}} \right)_{\text{Theory}} < 0.09 \quad (4.14)$$

That is, the experimentally determined hot press to sinter core-shell slope ratio is on the upper end of the range that would be expected from the model. The favorable comparison between the theoretical prediction and the experimental determination of the core-shell slope ratio supports the contention is the applied pressure of hot press processing is a significant factor in developing composition core shell structures in liquid phase sintering of compositionally mixed powders.

Chapter 5 Conclusion

Hitachi have developed a complex diffusion treatment of bulk high temperature magnets that produces $(\text{Nd}_x\text{Dy}_{1-x})_2\text{Fe}_{14}\text{B}$ grains with much of the Dy concentrated on the grain boundary layer, producing an enriched Dy shell about a Dy poor grain core. The objective of this thesis was to form a Hitachi-like Dy compositional core shell grain structure by consolidating mixed Dy rich and Nd rich powders. However, the consolidation of mixed Dy-rich and Nd-rich powders by liquid phase sintering for the purpose of forming compositional core shell structures is hampered by rapid homogenization of the Dy composition in the $(\text{Nd})_2\text{Fe}_{14}\text{B}$ grains during the densification process. Analysis of the activation energy for homogenization during consolidation suggests that diffusion through the liquid phase is the rate controlling step. This low activation energy is consistent with other alloy systems undergoing liquid phase sintering having transient liquid phase compositions, where the rationalization is that dissolution/precipitation in the liquid phase contributes to alloy homogenization. The hypothesis was developed that an acceleration of the consolidation process using applied pressure (hot pressing) would result in a reduced degree of Dy composition homogenization because the driving force for densification under applied pressure is magnified to a greater extent than the driving force for homogenization. Examination of the phase plane consisting of the coefficient of variance of the Dy composition vs the

relative density for liquid phase sintering with and without applied pressure shows a statistically significant difference between the two processes, with the Dy composition variance increased under hot press conditions. Direct visualization of the Dy composition core shell structure in the hot press samples is achieved by the independent techniques of EDS chemical mapping and backscatter imaging. These imaging techniques are validated by quantitative EDS point analysis. A simple model was developed which concludes that the ratio of normalized (Dy homogenization rate)/(consolidation rate) is determined by $(\frac{\Sigma}{\Sigma + P_{\text{applied}}})$ where Σ is the sintering stress and P_{applied} is the hot press applied pressure.

References

- [1] United States Patent, Patent No. : US8187392 B2, “R-Fe-B type rare earth sintered magnet and process for production of the same”;
- [2] United States Patent, Patent No. : US8206516 B2, “R—Fe—B rare earth sintered magnet and method for producing same”;
- [3] United States Patent, Patent No. : US20140271323 A1, “Manufacturing Nd-Fe-B Magnets Using Hot Pressing with Reduced Dysprosium or Terbium”;
- [4] Hongpo Shen, “Chinese tighten supply of rare earths as Terbium and Dysprosium prices soar”, *Technology Metals Intel*;
- [5] “New Alloying Process by Grain Boundary Diffusion”, *ShinEtsu Rare Earth Magnets*;
<http://www.shinetsu-rare-earth-magnet.jp/e/rd/grain.html>
- [6] Hiroyuki Suzuki, Yuichi Satsu, and Matahiro Komuro, “Magnetic Properties of A Nd-Fe-B Sintered Magnet with Dy Segregation”, *Journal of Applied Physics*, 2009, Vol 105, 07A734;
- [7] C. T. S. Tsai D.S., Hsu S.E., Hung M.P., Fe-Nd-B phase diagram, *Alloy Phase diagram DatabaseTM*;

- [8] Sheng Da, Liu Jincheng, “Cast Irons Containing Rare Earth”, *Tsinghua University Press*;
- [9] W.F. Li, H. Sepehri-Amin, T. Ohkubo, N. Hase, K. Hono, “Distribution of Dy in high-coercivity (Nd,Dy)–Fe–B sintered magnet”, *Acta Materialia*, 2011, Vol59, pp 3061–3069.
- [10] Ristić Momčilo M., Milosević S.D., “Frenkel theory of sintering”, *Science of Sintering*, 38 (2006) 7-11,
- [11] https://en.wikipedia.org/wiki/Propagation_of_uncertainty
- [12] David A. Atwood, “The Rare Earth Element: Fundamentals and Applicants”;
- [13] M. Chu, “Sintering Stress and Microstructure in Ceramic Powder Compacts”, *University of California-Berkeley*, pg. 33, 1990;
- [14] R. Raj, “Analysis of the Sintering Pressure”, *Journal of the American Ceramic Society*, 70 1987, p.c. 210;
- [15] H. Su and D.L. Johnson, “A Practical Approach to Sintering”, *Journal of the American Ceramic Society*, 1996, vol. 79, pg. 3211-3217;
- [16] Park et al, S.J. Park, S.H. Chung, J.M. Martin, John L. Johnson, R. M. German, “Finite Element Simulation of Liquid Phase Sintering with Tungsten Heavy Alloys”, *Materials Transactions*, Vol. 47, No. 11 (2006) pp. 2745 to 2752

- [17] Randall M. German, S.J. Park, S.H. Chung, J. M. Martín, John L. Johnson, “Master Sintering Curve for Densification Derived from a Constitutive Equation with Consideration of Grain Growth: Application to Tungsten Heavy Alloys”, *Metallurgical and Materials Transactions A*, Volume 39A, Dec 2008-2941
- [18] J.M. Vieira, R.J. Brook, “Kinetics of Hot pressing: The Semilogarithmic Law,” *Journal of the American Ceramic Society*, 1984, Vol.67 (4), pp.245-249;
- [19] De Campos, Marcos Flavio, “Diffusion Coefficients of Interest for the Simulation of Heat Treatment in Rare-Earth Transition Metal Magnets”, *Materials Science Forum*, 2012, Vol.727-728, pp.163-168;
- [20] Jean-Paul Poirier, *Introduction to the Physics of the Earth's Interior Cambridge Press*, 2000, pp 188;
- [21] Bharat B.Panigrahi, N.Subba Reddy, Karabi Das, M.M.Godkhindi, “Dilatometric Sintering of Ti-2Al and Ti-5Al Elemental Powder”, *Journal of Material Science & Technology*, Vol 23, (03), 2007
- [22] Ekbom L., Antonsson T. and Ekbom M., “Computer simulation of solution and growth processes during the initial stage of liquid phase sintering of tungsten heavy metal”, *Scandinavian Journal of Metallurgy*, 2005, Vol.34 (5), pp.312-316;
- [23] W.H. Rhee, D. N. Yoon, “The instability of solid-liquid interface in MoNi alloy

induced by diffusional coherency strain” *Acta Metallurgica*, 1987, Vol.35(7), pp.1447-1451;

[24] Rahaman, M.N., De Jonghe, L.C., and Brook, R.J., “Effect of shear stress on sintering”, *Journal of the American Ceramic Society*, 1986, Vol 69, pp 53-58;

[25] Sean M. Sweeney and Merrilea J. Mayo, “Green Density-based Sintering Predictions”, *Journal of Materials Research*, 2002, Vol. 17, pp 89-97;

Appendix A Time, temperature and process comparison of experiment matrix

Table Appendix A.1 data comparison of experiment matrix_1

Label in Fig 4.4	Label	Sample process (hot press)	Mill time	Papp(mp/min)	Hot press(t/mins)	Papp(heat after hot press)
I	86.5 900C 1h	Heat the hot pressed sample for 1h at 900C for	DMC with Dy ₂ 34Fe 5mins	37.8	13	atm
J	92 900C 5h	Heat the hot pressed sample for 5hrs at 900C for GBDP (sp 850C)	DMC with Dy ₂ 34Fe 50 mins (Material Media 7.81)	47.5	42	atm
K	95 asp	Hot pressed sample (sp 850C)	DMC with Dy ₂ 34Fe(50m/s) 50 mins (17/1)	11.9	40	-----
M	95 600C 4h	Hot pressed sample (sp 850C) For 4 hrs at 600C	DMC with Dy ₂ 34Fe(50m/s) 50 mins (17/1)	11.9	40	atm
	99 asp	Hot pressed sample (sp 850C)	Nd ₂ Fe ₁₄ B powder with Dy ₂ 3Fe ₁₄ B powder 15	56.8	11	-----
	99 900C 24h	Hot pressed sample (sp 850C) Then 24 hrs at 900C	Nd ₂ Fe ₁₄ B powder with Dy ₂ 3Fe ₁₄ B powder 15 mins no media	56.8	11	atm
	99 900C 12h	Hot pressed sample (sp 850C) Then 12 hrs at 900C	Nd ₂ Fe ₁₄ B powder with Dy ₂ 3Fe ₁₄ B powder 15 mins no media	56.8	11	atm
L	97 asp	Hot pressed sample (sp 850C)	Dy ₂ 3Fe ₁₄ B powder with Nd ₂ Fe ₁₄ B ribbon 50mins(1/18)+15mins(1/1.16)	42.4	22	-----
	97 850C 2h	Hot pressed sample (sp 850C) Then 2 hrs at 850C	Dy ₂ 3Fe ₁₄ B powder with Nd ₂ Fe ₁₄ B ribbon 50mins(1/18)+15mins(1/1.16)	42.4	22	atm
	96 pressure 2h	Hot pressed sample(3B) (sp 850) Then heat under pressure 2hrs	Nd ₂ Fe ₁₄ B powder with Dy ₂ 3Fe ₁₄ B powder 15 mins no media	48.8	25	76.8
Label in Fig 4.4	Label	Sample process (sintering)	Mill time	Papp(mp/min)	Hot press(t/mins)	Papp(heat after hot press)
C	875 5h	Sinter at 875C, 5h	30%Dy powder + 70%Nd ₂ Fe ₁₄ B powder 15 mins no media	atm	-----	-----
D	900 5h	Sinter at 900C, 5h	30%Dy powder + 70%Nd ₂ Fe ₁₄ B powder 15 mins no media	atm	-----	-----
E	925 5h	Sinter at 925C, 5h	30%Dy powder + 70%Nd ₂ Fe ₁₄ B powder 15 mins no media	atm	-----	-----
A	1050 30m	Sinter at 1050C, 30mins	Dy ₂ Fe ₁₄ B flake Nd ₂ Fe ₁₄ B powder	atm	-----	-----
F	1050 5 h FP	Sinter at 1050C, 5 hrs	Dy ₂ Fe ₁₄ B flake Nd ₂ Fe ₁₄ B powder	atm	-----	-----
G	1050 5h PP	Sinter at 1050C, 5 hrs	Dy ₂ Fe ₁₄ B powder Nd ₂ Fe ₁₄ B powder	atm	-----	-----
B	675	Normal sintering	Fe ₁₄ B add to Nd ₂ Fe ₁₄ B ribbon 0.5mol	atm	-----	-----
H	LO2	LO2	Fe ₁₄ B/mol Nd liq Then mix with 30%Dy powder	-----	-----	-----
Label	Label	Sample	Mill time	Papp(mp/min)	Hot press(t/mins)	Papp(heat after hot press)
	4% Source	4% Source as pressed Then heat under pressure 1hrs	4%Dy mix powder Mill in Ar and in vetrel for 1.5mins	48.8	15	76.8
	4% homo	4% homogeneous Then heat under pressure 1hrs	4%Dy in DMC in grain	64.6	15	76.8
	4% homo+2% Source	4% homogeneous Dy + 2% Dy source	4%Dy in DMC in grain 2%Dy in source	65.5	28	-----

Table Appendix A.2 data comparison of experiment matrix_2

Label in Fig 4.4	Label	Variance coefficient	$\Delta t(h)$	P (% theoretical)	L(um)	Papp(mp/min)	Hot press(t/mins)	Papp(heat after hot press)
I	86.5 900C 1h	100	1	86.5	362±92	37.8	13	atm
J	92 900C 5h	100	5	92	238±26	47.5	42	atm
K	95 asp	100	0	95	228±130	11.9	40	-----
	95 600C 4h	81	4	95	225±46	11.9	40	atm
M	99 asp	91.8	0	99	134±29	56.8	11	-----
	99 900C 24h	70.7	24	99	145±29	56.8	11	atm
	99 900C 12h	75	12	99	144±40	56.8	11	atm
L	97 asp	100	0	97	100±28	42.4	22	-----
	97 850C 2h	92.3	2	97	114±29	42.4	22	atm
	96 pressure 2h	65.7	2	96	144±40	48.8	25	76.8
Label in Fig 4.4	Label	Variance coefficient	$\Delta t(h)$	P (% theoretical)	L(um)	Papp(mp/min)	Hot press(t/mins)	Papp(heat after hot press)
C	875 5h	43	5	81	200	atm	-----	-----
D	900 5h	37	5	82	200	atm	-----	-----
E	925 5h	26.5	5	84	200	atm	-----	-----
A	1050 30m	71.6	0.5	76	300	atm	-----	-----
F	1050 5 h FP	14	5	87	300	atm	-----	-----
G	1050 5h PP	14.3	5	87.3	200	atm	-----	-----
B	675	60.6	0	78.9	200	atm	-----	-----
H	LO2	16	-----	90	3000	-----	-----	-----
Label	Label	Variance coefficient	$\Delta t(h)$	P (% theoretical)	L(um)	Papp(mp/min)	Hot press(t/mins)	Papp(heat after hot press)
	4% Source	65.7	1	99	144±40	48.8	15	76.8
	4% homo	0	1	97	-----	64.6	15	76.8
	4% homo+2% Source	24.6	0	99	-----	65.5	28	-----

Appendix B The analysis of Ψ in equation 4.8(a)

Table Appendix B.1 Analysis of Ψ

Chemistry-Process	Sintering Stress Range MPA	Technique	Reference
SiC-Solid State Sinter	0.5-3.0	Model Calculation	T. Kraft, H. Riedel, Journal of the European Ceramic Society 24 (2004) 345–361
YBa ₂ Cu ₃ O ₆ -solid state Sinter	0.4	Creep Densification rate ratio	M. Rahaman, L. DeJonghe, LBL-24764 Preprint, 1988
Cu powder-Solid State Sinter	0.2	Tensile Stress	R.A. Gregg and F.N. Rhines, "Surface Tension and the Sintering Force in Copper," <i>Metallurgical Transactions</i> , vol. 4, 1973, pp. 1365-1374.
MgO-Bi ₂ O ₃ -Liquid Phase Sintering	0.78	Creep Densification Rate Ratio	L. DeJonge, V. Srikanth, LBL-243 1 1 Preprint, 1988
General Supersolidus LPS	~1.0	unknown	https://www.cavs.msstate.edu/publications/docs/2003/07/2003-15.pdf
Bronze Supersolidus LPS	1.4	unknown	R. Tandon, Ph. D. Thesis, Pennsylvania State University, University Park, PA, December 1995.

It is often proposed that the variation of rate of relative density change with time can be described by the simple relationship

$$\frac{d}{dt} \rho * \frac{1}{\rho} = \frac{H * D * \Omega * \Phi(t)^m * (\Sigma(t) + P_{\text{applied}})}{k * T * G(t)^n}$$

ρ is density, H is constant, D is diffusion coefficient, Ω is atomic volume, $\Phi(t)$ is the time dependent stress intensification factor, $m=2$ for grain boundary diffusion and $m=1.5$ for volume diffusion. $\Sigma(t)$ is the time dependent sintering stress, P_{applied} is the applied pressure (hot pressing). G is time dependent grain size, $n=2m-1$, k is Boltzmann's

constant and T is temperature.

This suggests a solution of the form

$$\frac{\rho}{\rho_{th}} = \frac{\rho_0}{\rho_{th}} * \exp\left(\frac{H*D*\Omega}{k*T} * \int_0^t \frac{\Phi(\tau)^m * (\Sigma(\tau) + P_{applied})}{G(\tau)^n} d\tau\right) \quad (B.1)$$

Where ρ_0 is the initial (green) density. The integral in equation B.1 is evidently difficult to predict, even upon the assumption of a constant sintering stress, as empirical relationships between time and density are often proposed. A semi-log relationship is often used for the empirical analysis between density and time. However, this offers a poor empirical fit at short times because it predicts an infinite slope at the initial ($t=0$) stage of sintering. An alternative is to use an empirical expression of the form:

$$\frac{\rho}{\rho_{th}} = \frac{\rho_0}{\rho_{th}} \exp\left(\frac{H*D*\Omega}{k*T} \int_0^t \frac{\Phi(\tau)^m \Sigma(\tau)}{G(\tau)^n} d\tau\right) = 1 - \frac{\rho_{th} - \rho_0}{\rho_{th}} \exp\left[-\left(\frac{H*D*\Omega*\Psi}{k*T} * t\right)\right] \quad (B.2)$$

Which can closely match semi-log behavior while still describing reasonable behavior at $t=0$. In fact, considering the sintering rate at $t=0$ provides a definition for the mysterious parameter Ψ . Taking the derivative with respect to time of both sides of equation B.2 and examining $t=0$ gives

$$\frac{\rho_0 * \frac{\Phi(0)^m \Sigma(0)}{G(0)^n}}{(\rho_{th} - \rho_0)} = \Psi \quad (B.3a)$$

for sintering and

$$\frac{\rho_0 * \frac{\Phi(0)^m (\Sigma(0) + P_{applied})}{G(0)^n}}{(\rho_{th} - \rho_0)} = \Psi \quad (B.3b)$$

for hot pressing.

That is, Ψ is proportional to a function that describes the initial configuration of the

powder pack through the initial (green) density, sintering stress and grain size (or diffusion length). It is known that sintering kinetics are strongly dependent on the initial configuration of the powder pack and in that sense the approximation is consistent with physical behavior. Moreover, it is known [24] that the initial sintering rate is accelerated as the green density increases or the grain (particle) size decreases, which is in fact consistent with equations B.2 and B.3.

Appendix C Copyright permission for Figure 2.1

INTERNATIONAL COPYRIGHT PERMISSION REQUEST

Please complete all contact information:

Name: Li Chen Title:
Company/Organization: Michigan Technological University
Address: 32087 Hamilton Ct Apt A 201
City/State/Zip/Country: Solon OH 44139 US
Phone: 9063702581 Email: lchen2@mtu.edu

I am preparing an article/chapter for publication in the following formats (check as applicable):

Print Only ☐ Internet Only ☐ Print and Electronic Media ☒

The information will be used for (check as applicable):

Journal article ☐ Conference presentation ☐ Internal company records ☐
Dissertation ☒ Student course material ☐ Commercial publication* ☐

Please complete the following:

The article/chapter title will be: Chapter 2 Background, Objective and Hypothesis

The publication title will be: Nd₂Fe₁₄B: (Nd_{1-x}Dy_x)₂Fe₁₄B CORE-SHELL STRUCTURE FORMATION BY HOT PRESS LIQUID

Publisher: Michigan Technological University, ProQuest

Planned date of publication: April 1st, 2016

I hereby request permission for non-exclusive world rights for the above publication and all subsequent editions, revisions, and derivative works in English and foreign translations, in the formats indicated above from the following copyrighted content by **ASM International**:

Book ISBN:

Copyright date: 2006-2016

Book/Publication title: Alloy Phase Diagram Database TM

Author name(s): Zhang N., Yang L.

Article title: Phase diagram of Nd-Fe-B ternary system: Two vertical sections with constant Nd and B respectively, passing through Nd₂

Text page numbers:

Figure numbers (with page numbers): Unique ID No. 978568

Table numbers (with page numbers):

Signature:

Li Chen

Date: 2/22/2016

FOR ASM INTERNATIONAL USE ONLY:

I (we) grant permission requested above. Please ensure that ASM International receives proper credit as publisher by citing the above ASM publication as a reference and including the following: Reprinted with permission of ASM International. All rights reserved.

ASM International Representative: Sue Sellers

Digitally signed by Sue Sellers
DN: cn=Sue Sellers, o=ASM International, ou=Permissions,
email=sue.sellers@asminternational.org, c=US
Date: 2016.02.23 11:08:29 -0500

Date: 02-23-2016

*For Commercial Publications, a copyright permission fee of \$50 per figure will be assessed.
Exceptions can be made for reuse of content by its original authors.

ASM International, Permissions, 9639 Kinsman Road, Materials Park, Ohio 44073-0002
, Phone: 440-338-5151 x5465, Fax: 440-338-8542

SUBMIT